

Journal of Geophysical Research: Solid Earth

RESEARCH ARTICLE

10.1029/2017JB015289

Key Points:

- We performed a multiscale, radially anisotropic waveform inversion at periods from 30 to 120 s
- A fully automated inversion procedure enables the incorporation of large-scale data sets
- The 20 L-BFGS iterations result in a model that explains complete waveforms

Correspondence to:

L. Krischer,
lion.krischer@erdw.ethz.ch

Citation:

Krischer, L., Fichtner, A., Boehm, C., & Igel, H. (2018). Automated large-scale full seismic waveform inversion for North America and the North Atlantic. *Journal of Geophysical Research: Solid Earth*, 123, 5902–5928. <https://doi.org/10.1029/2017JB015289>

Received 30 NOV 2017

Accepted 7 APR 2018

Accepted article online 17 APR 2018

Published online 28 JUL 2018

Automated Large-Scale Full Seismic Waveform Inversion for North America and the North Atlantic

Lion Krischer^{1,2} , Andreas Fichtner¹ , Christian Boehm¹ , and Heiner Igel² 

¹Department of Earth Sciences, Institute of Geophysics, ETH Zurich, Zurich, Switzerland, ²Department of Earth and Environmental Sciences, Ludwig-Maximilian University of Munich, Munich, Germany

Abstract We present a new anisotropic seismic tomography model based on a multiscale full seismic waveform inversion for crustal and upper-mantle structure from the western edge of North America across the North Atlantic and into Europe. The gradient-based inversion strategy utilizes the adjoint state method coupled with an L-BFGS quasi-Newton optimization scheme. To improve the handling of large data quantities in the context of full seismic waveform inversions, we developed a workflow framework automating the procedure across all stages, enabling us to confidently invert for waveforms from 72 events recorded at 7,737 unique stations, resulting in a total of 144,693 raypaths, most of them with three-component recordings. The final model after 20 iterations is able to explain complete waveforms including body as well as surface waves of earthquakes that were not used in the inversion down to periods of around 30 s. The model is complemented by a detailed resolution analysis in the form of 3-D distributions of direction-dependent resolution lengths.

1. Introduction

Inversions for volumetric elastic properties of the Earth's subsurface using seismic data face the difficult task of using point-localized, and often uneven, surface measurements. Densely populated areas in developed countries that are exposed to seismic risk tend to be densely instrumented, whereas large parts of the planet (e.g., oceans and deserts) are lacking in terms of seismic recordings, though efforts to change this are underway (Sukhovich et al., 2015). Furthermore, data contain environmental and instrument noise, potentially strong effects of the local subsurface, and plain errors arising from technical or operational issues. Having more data has the potential to alleviate both these problems by (a) covering previously uncovered areas and (b) statistically averaging to reduce the importance of errors and certain local effects like timing errors of seismic receivers, for example.

Following the pioneering traveltime inversions of Dziewoński et al. (1977) and Aki et al. (1977), seismic tomography has advanced substantially through the growing quality and quantity of data and also thanks to methodological developments. The latter include various forms of finite-frequency tomography (e.g., Dahlen et al., 2000; Friederich, 2003; Li & Romanowicz, 1996; Sigloch et al., 2008; Yomogida, 1992; Yoshizawa & Kennett, 2004, 2005), joint inversions of body and surface wave data (e.g., Koelemeijer et al., 2017; Ritsema et al., 1999, 2011), and sophisticated sampling strategies (e.g., Bodin & Sambridge, 2009; Sambridge & Drijkoningen, 1992).

Today's computational resources enable us to invert "full" waveforms using numerical forward and adjoint simulations of wave propagation through the complex 3-D Earth. Based on theoretical foundations that were developed early on (e.g., Bamberger et al., 1977, 1982; Tarantola, 1988), recent full-waveform inversions have been conducted from local to global scales (e.g., Bozdag et al., 2016; Colli et al., 2013; Çubuk Sabuncu et al., 2017; French & Romanowicz, 2014; Prieux et al., 2013; Tape et al., 2010; Zhu et al., 2012).

With many technical details of full-waveform inversion being meanwhile well established, a remaining challenge still lies in the incorporation of large quantities of data, as provided, for instance, by the USAArray project (<http://www.usarray.org>, last accessed November 2017). Responding to this challenge, the focus of this work is the development of a scalable and automated full-waveform inversion procedure. This includes various technical advances in the form of the ObsPy toolkit (Beyreuther et al., 2010; Krischer, Megies, et al., 2015; Megies et al., 2011) to more efficiently process data, the Large-Scale Seismic Inversion Framework

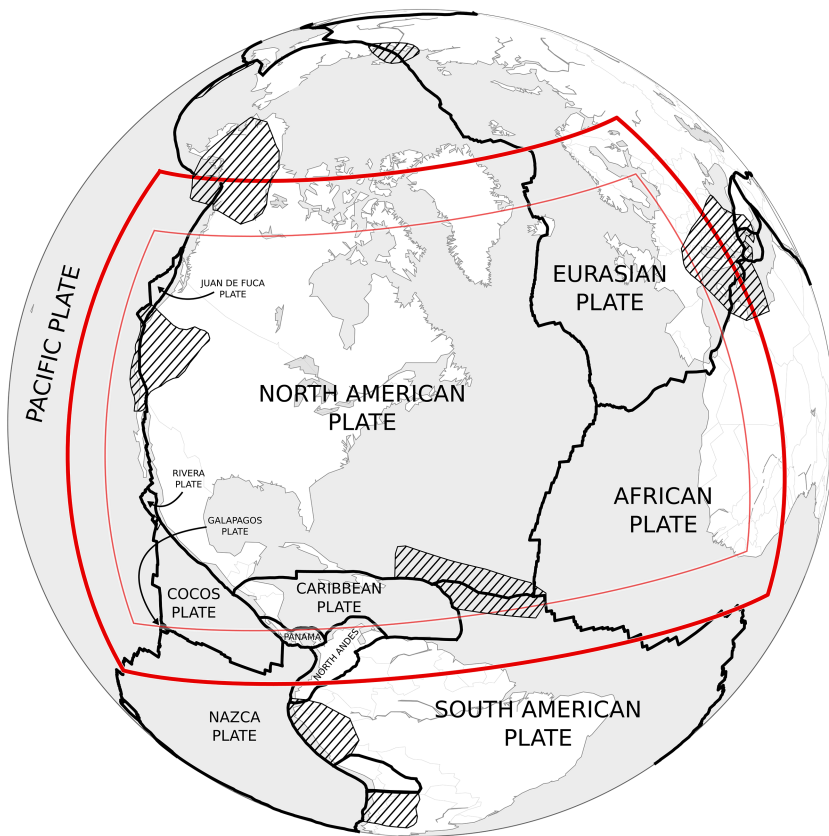


Figure 1. The inversion domain and its tectonic setting. The outer red boundary marks the full domain in which we ran our simulations and inversion procedure. In order to mitigate the effects of the necessary, but unphysical, absorbing boundaries on the inversion, we only use data whose direct raypaths are within the inner red boundary. The black lines show the tectonic plate boundaries, and the hatched areas are orogens where a further microzonation in smaller tectonic plates is not performed. Plate boundaries and orogens are taken from Bird (2003).

(LASIF; Krischer, Fichtner, et al., 2015) to aid in managing data in the context of full seismic waveform inversions, and the Adaptable Seismic Data Format (ASDF, Krischer et al., 2016) to support storing and exchanging data. A graph-based workflow orchestration framework has been developed to couple these tools to a numerical optimization library resulting in an inversion procedure that can run without human intervention.

To ensure the functionality of our developments, we perform a full-waveform inversion for North America and the North Atlantic. Figure 1 shows our study region. It contains the complete continental United States and has been expanded to the west, south, and east in order to include tectonic boundaries granting access to data from additional earthquakes large enough to be used for the inversion. Moreover, the study region contains a significant part of western Europe to take advantage of the dense instrumentation in that region. Diverse tectonic settings from the subducting plates beneath the west coast of North America, over the complex structure under the Caribbean Sea, to the Mid-Atlantic Ridge, including the Iceland hot spot, provide ample reasons to study this domain in as much detail as possible.

The remainder of the manuscript is structured as follows. Section 2 details the chosen forward and inverse modeling scheme, followed by an overview of the data in section 3. Results and resolution proxies are presented in section 4, with potential next steps being discussed in sections 5 and 6.

2. Forward and Inverse Modeling

Our waveform modeling and inversion largely follows the methodology established in Fichtner et al. (2009), Fichtner (2011), Tape et al. (2010), and similar works. The main difference are various technical efforts to scale the inversion to more data, which are detailed in the following sections.

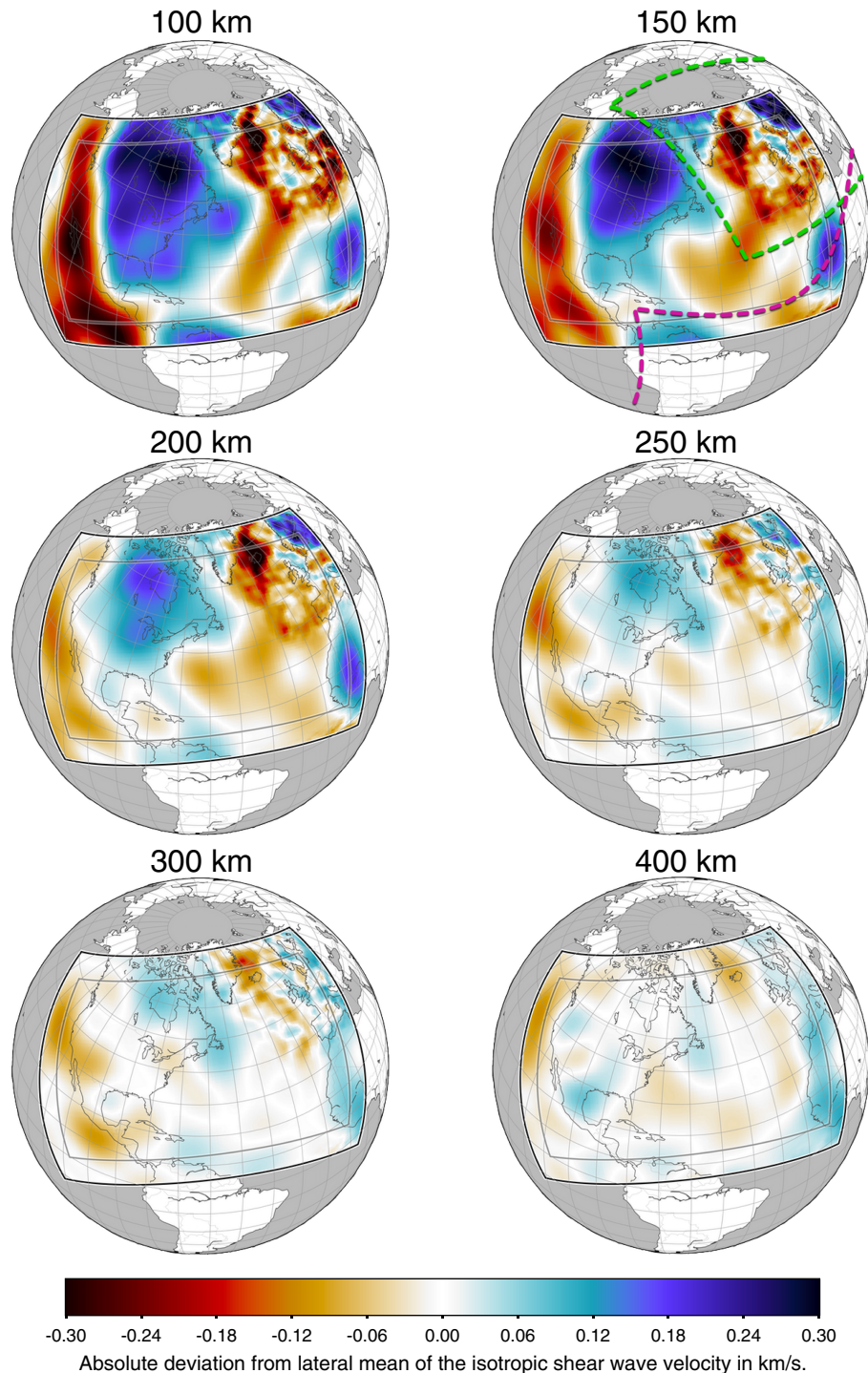


Figure 2. Horizontal slices through the initial model showing the isotropic shear wave speed at various depths with the same color scale. The slice at a depth of 150 km additionally shows the two existing full-waveform inversion models that are part of the initial model: The green dashed border is an outline of a model for Europe from Fichtner et al. (2013), and the purple dashed border denotes the extent of the South Atlantic model from Colli et al. (2013).

2.1. Waveform Modeling and Starting Model

Solutions of the linear viscoelastic wave equation and its adjoint in a radially anisotropic medium are computed using SES3D (Gokhberg & Fichtner, 2016). It employs the spectral-element method (Faccioli et al., 1997; Komatitsch, 1997; Seriani et al., 1995), which, in addition to its computational efficiency, has natural free surface boundary conditions, a useful trait for modeling surface wave-dominated data. Long-period effects like self-gravitation are not simulated, neither full gravity nor Cowling's approximation, limiting the longest period to around 120 s.

Gradient-based optimization mandates a good starting model, which has been extracted from the Collaborative Seismic Earth Model (CSEM; Afanasiev et al., 2016). It consists of a global 1-D background model based on Preliminary reference Earth model (PREM; Dziewoński & Anderson, 1981) including its attenuation model with the discontinuity at a depth of 220-km being replaced by a linear gradient, superimposed by 3-D perturbations of S velocity from S20RTS (Ritsema et al., 1999). Perturbations of P velocity are scaled to S velocity using the relations of Ritsema and van Heijst (2002). Globally, the crust is derived from the model of Meier et al. (2007). Our inversion domain additionally contains contributions from full seismic waveform models of Europe (Fichtner et al., 2013) and the South Atlantic (Colli et al., 2013). These can be clearly seen in the initial model in Figure 2. The final result of this work flows back into the Collaborative Seismic Earth Model so it can serve as a foundation for future generations of Earth models.

2.2. Optimization Scheme

Our wave propagation simulations use models parameterized in vertically and horizontally propagating/polarized P and S velocity, v_{PH} , v_{PV} , v_{SH} , v_{SV} , density ρ , shear attenuation Q_μ , and the dimensionless parameter η (Dziewoński & Anderson, 1981), which controls the incidence-angle-dependent speed of seismic waves. Independently constraining all these parameters is not realistic with the given data coverage. Thus, we invert only for the isotropic P velocity v_p , and for v_{SH} , v_{SV} , and ρ . To reduce the parameter space, we force $\eta = 1$ and $v_{PH} = v_{PV}$. See Fichtner et al. (2013) for a more detailed explanation and reasoning. Parameters are defined at the quadrature points of the numerical mesh with a built-in smoothing operator as detailed below.

Density anomalies may be poorly constrained as their effect on the seismic wavefield is comparatively small. It can be shown that ignoring density during an inversion negatively affects the recovery of the other parameters (Blom et al., 2017). Hence, we include density in the optimization but do not interpret it.

The model is updated by calculating the gradient of the objective functional—explained in more detail in section 2.3—with respect to the model parameters using the adjoint state method (Fichtner et al., 2006; Tape et al., 2007; Tarantola, 1988; Tromp et al., 2005). The gradients drive an L-BFGS method (Liu & Nocedal, 1989) to iteratively compute updates. L-BFGS is a quasi-Newton method that includes curvature information based on approximations of the inverse Hessian constructed from the gradients and models of previous iterations. This method is matrix free and only requires few vector-vector operations, which makes it attractive for solving large-scale inverse problems. Our implementation differs from the classical text book algorithm Nocedal and Wright (2006) by including a Gaussian smoothing operator into the parameterization of the model and the initialization of L-BFGS. This yields a consistent discrete gradient, which is necessary to avoid restarts of the L-BFGS history caused by inaccurately computed search directions. Details can be found in Appendix A.

L-BFGS has two main advantages over conjugate gradient methods, which both lower the cost of waveform inversion by reducing the number of required simulations. First, the proposed model update is automatically scaled, which usually avoids additional simulations to compute the step length for line-search methods. Second, the rate of convergence is higher, thus requiring fewer iterations to approach the final model (Modrak & Tromp, 2016).

Seismic wave propagation is a global phenomenon, but we only model it in a limited spatial domain and thus have to be careful to avoid boundary effects. A buffer zone, about 2 to 3 times the width of the area with active perfectly matched layers, is allocated along all domain borders. We discard all data that have direct raypaths crossing that boundary zone and also taper our gradients so they are largely zero within the boundary region.

2.3. Misfit Functional

The concrete choice for the objective functional $\chi(\mathbf{m})$ for the seismograms from a particular model \mathbf{m} has a large influence on the outcome of an inversion. It determines if and how observed and synthetic data have to be windowed and what seismic phases can be used. Long-wavelength Earth structure mainly speeds up or slows down seismic waves, and using the L^2 distance between observed and synthetic data does not explicitly

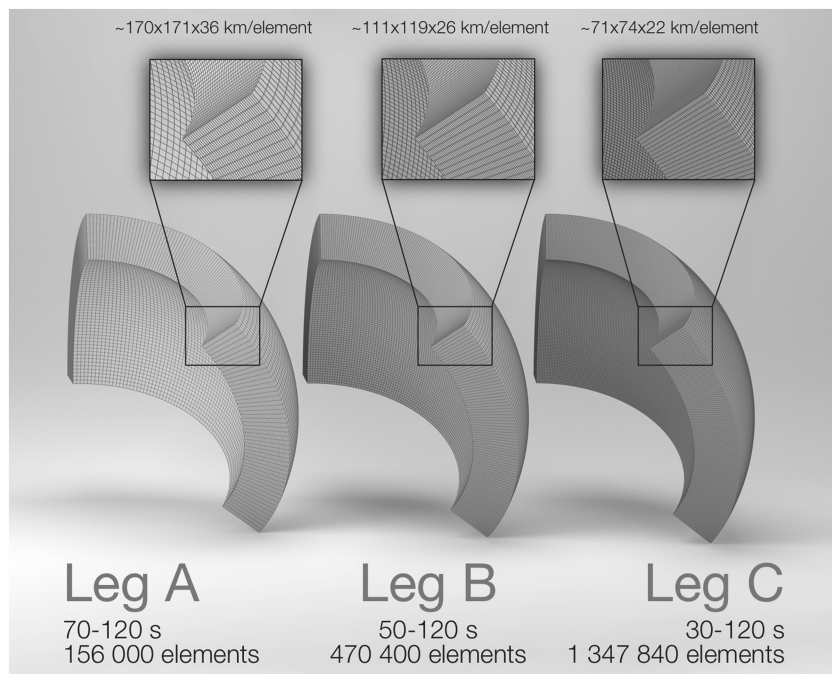


Figure 3. The numerical meshes used for the different legs of the inversion. The smaller elements of leg C compared to leg A also necessitate a smaller time step. As a consequence, a single iteration of leg C is more than 20 times as expensive as a single iteration for leg A. Element dimensions at the top are given in approximate kilometer per element in latitude/longitude/depth directions.

extract such traveltime information. Luo and Schuster (1991) argue that a cross-correlation time shift misfit functional has a more linear relationship with the model parameters. Alternatives are frequency-dependent multitaper measurements (e.g., Tape et al., 2007; Thomson, 1982), and instantaneous phase and envelope misfits (Bozdağ et al., 2011; Rickers et al., 2012).

Here we work with the closely related phase misfit measured in the time-frequency domain, as introduced by Fichtner et al. (2009). It is based on the transformation of both observed and synthetic seismograms to the time-frequency domain, where differences in phase are measured. A particular advantage of this approach is that individual seismic phases need not be identified and isolated. A downside is that careful window selection is essential to avoid cycle skips, especially at higher frequencies. The total phase misfit χ_p^2 is defined by an integral over all phase differences in the time-frequency domain as

$$\chi_p^2 = \iint W^2(t, \omega) [\phi_{\text{syn}}(t, \omega) - \phi_{\text{obs}}(t, \omega)]^2 dt d\omega, \quad (1)$$

with W being the weighting function and ϕ_{syn} and ϕ_{obs} the phase of the synthetic and the observed seismogram trace, respectively. For a derivation and the corresponding adjoint source, the reader is referred to Fichtner et al. (2009) and Fichtner (2011).

Windows have been automatically selected by an algorithm utilizing a sliding window cross correlation. This yields time-dependent cross-correlation coefficients and time shifts which are combined with further criteria to select the final windows. The procedure is described in more detail in Krischer, Fichtner, et al. (2015), and the results are illustrated in section 3.

2.4. Multiscale Inversion

To avoid trapping in a local minimum, we follow the common approach of starting with longer periods to determine large-scale structure before going to shorter periods (e.g., Bunks et al., 1995; Fichtner, 2011). Specifically, we divide the inversion into three legs:

1. **Leg A:** Periods from 70 to 120 s
2. **Leg B:** Periods from 50 to 120 s
3. **Leg C:** Periods from 30 to 120 s

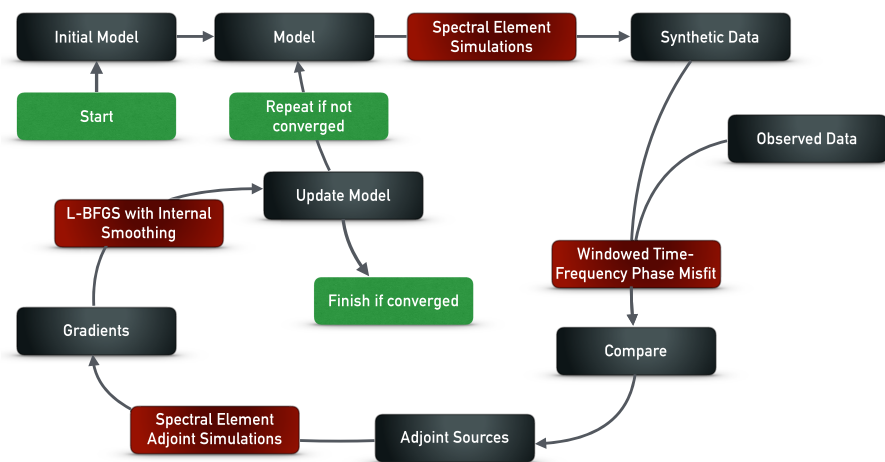


Figure 4. Schematic workflow for full seismic waveform inversions. Starting from an initial model, observed and synthetic data from that model are compared to obtain the gradient of the misfit with respect to the model parameters. This is then used to update the model to reduce the discrepancy between both. Repeat until converge or the risk of overfitting becomes too large. Dark gray boxes are the different elements that enter a full-waveform inversion using adjoint techniques, red boxes are implementation details with the choices taken in this study, and green boxes denote the start and end of an iteration.

Figure 3 shows the finite-element meshes used for the different period legs. The L-BFGS optimization has to be restarted each time the definition of the misfit functional changes, for example, when the frequency content is modified. We use the transitions to shorter periods as an opportunity to introduce more data into the inversion. The Gaussian smoothing operator of the inversion model's parameterization has a horizontal sigma ranging from 350 to 150 km and a vertical sigma ranging from 70 to 30 km going from leg A to leg C. Further details concerning data are provided in section 3.

2.5. Workflow Management

While full-waveform inversions using adjoint methods have been applied for more than 20 years (e.g., Bozdağ et al., 2016; Chen et al., 2007; Colli et al., 2013; Fichtner et al., 2009; Igel et al., 1996; Rickers et al., 2013; Simute et al., 2016; Tape et al., 2010; Zhu et al., 2012, 2017), a major difficulty lies in the large quantities of today's available data, and the required data management and workflow orchestration, which is elaborated upon in this section.

The simplified workflow depicted in Figure 4 does not capture all the complexity of the task, as recorded data has to be downloaded, instrument corrected, and filtered to match the spectral content of the synthetics, the simulations have to be set up, launched, and monitored, one forward and one adjoint simulation per event and per iteration. Suitable windows have to be chosen in which observed and synthetic data are similar enough to enable a physically meaningful comparison. Potentially weighted misfits and adjoint sources have to be derived for each window. The resulting adjoint sources have to be converted to a format the wave equation solver can read and stored in a place it can access. Gradients from separate events have to be read and summed. These and various other tasks have to be dealt with in a reliable and trustworthy manner, which in this study is done by LASIF (Krischer, Fichtner, et al., 2015).

Adjoint simulations require access to the wavefield from the forward runs which is often done by storing the forward wavefield every few time steps and interpolating in-between. For high-frequency simulations and many events, the temporary storage costs become prohibitive and on the order of several 100 TB per iteration for this study. To reduce this load, we employ a simplified version of the wavefield compression introduced in Boehm et al. (2016) by storing the forward wavefield only at a polynomial degree of 2 (instead of 4 which is used for the simulations) and by using a variable number of bits per element depending on the maximum absolute value of the wavefield. This reduces the storage cost to about 10 TB for our study which is manageable on modern high-performance platforms. An alternate approach is checkpointing (see, e.g., Anderson et al., 2012; Griewank, 1992; Symes, 2007), which can be tuned to use very little storage but increases the cost of gradient calculations by one third.

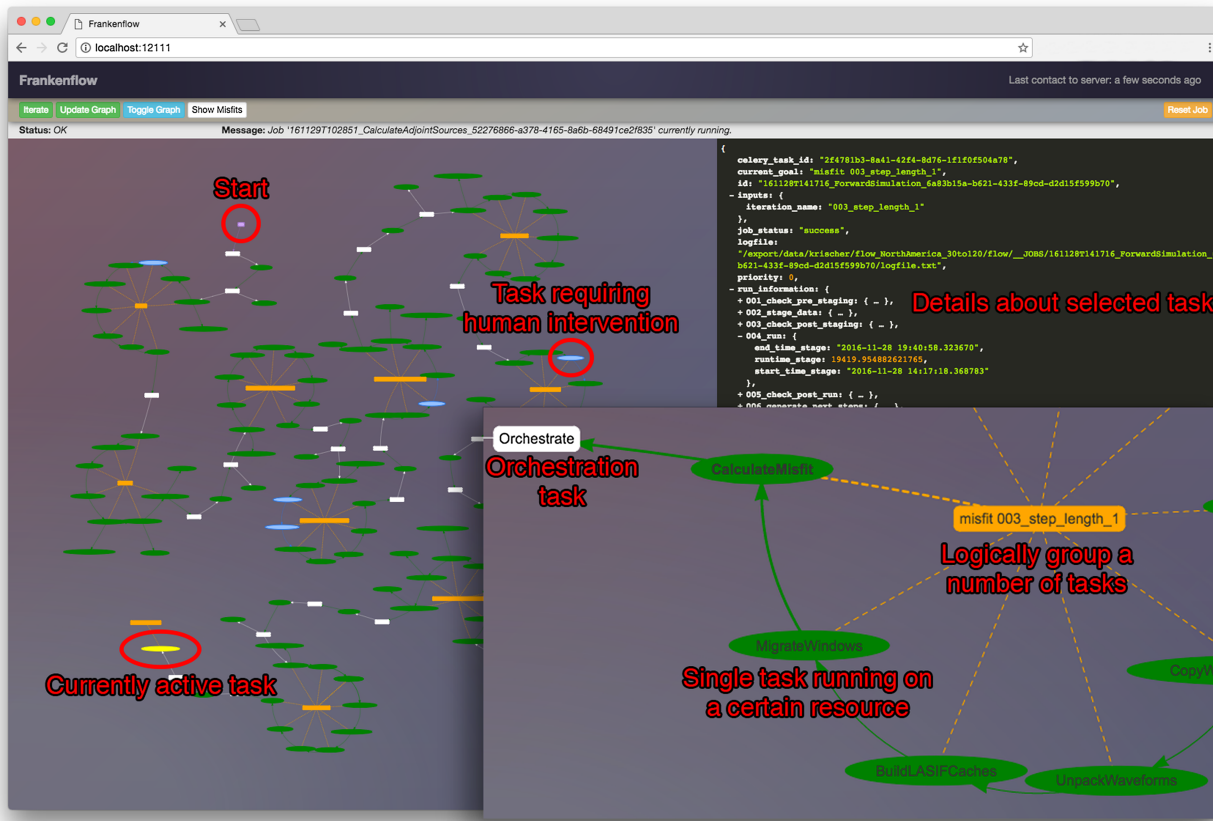


Figure 5. Screenshot of the graphical interface to the graph-based workflow orchestration tool developed for the inversion. The inlay on the bottom right is a zoomed in version of the graph; all red elements are annotations not part of the actual interface. The directed graph on the left-hand side ties together single tasks (green nodes), which are executed on various different computational resources. The orange nodes group tasks around higher order goals to facilitate reading the graph. White nodes portray orchestration tasks which are used to either call the optimization toolbox or to parse its output to decide what to do next. Light blue nodes finally denote tasks which failed automatic completion and required human intervention for a variety of reasons.

Widely available nonlinear optimization toolboxes (e.g., Jones et al., 2001–; Wächter & Biegler, 2005) mostly assume that the forward problem and derivatives of the objective functional can be calculated quickly; their interfaces work with some form of callback functions. This is not the case with full-waveform inversions where a single gradient calculation can take thousands of node hours. These tools are thus not directly applicable. L-BFGS necessitates access to the gradients of previous iterations and manually arranging this proves to be error prone. These two issues motivated the development of a graph-based workflow orchestration tool tuned for numerical optimization in the context of full seismic waveform inversions.

At its core is the L-BFGS algorithm with a built-in Gaussian smoothing operator as described in section 2.2. Depending on the current state of the optimization procedure, it will request either the misfit, the gradient, or both for the current model realization. This will trigger a sequence of steps, which involves calling the proper functionalities of LASIF, launching simulations on high-performance machines, copying and merging gradients, calculating adjoint sources and misfits, and returning the results to the optimization toolbox. Some of these operations can take hours to days, and everything is thus handled in a fully automated fashion where tasks are executed according to a defined graph structure and dispatched with a job queuing system. This graph is stored and facilitates reproducibility. A browser-based interface to monitor, visualize, and interact with the graph has been developed and is presented in Figure 5. Among other things it can be used to pause the workflow and also restart from a given state to recover from failures. These include the high-performance computer being in maintenance, an exceeded disc quota, partially completed jobs, and a workstation being out of memory due to L-BFGS runs at a fine-model resolution using multiple gradients. Any workflow handling large amounts of data and running big simulations will encounter these or other errors and the ability

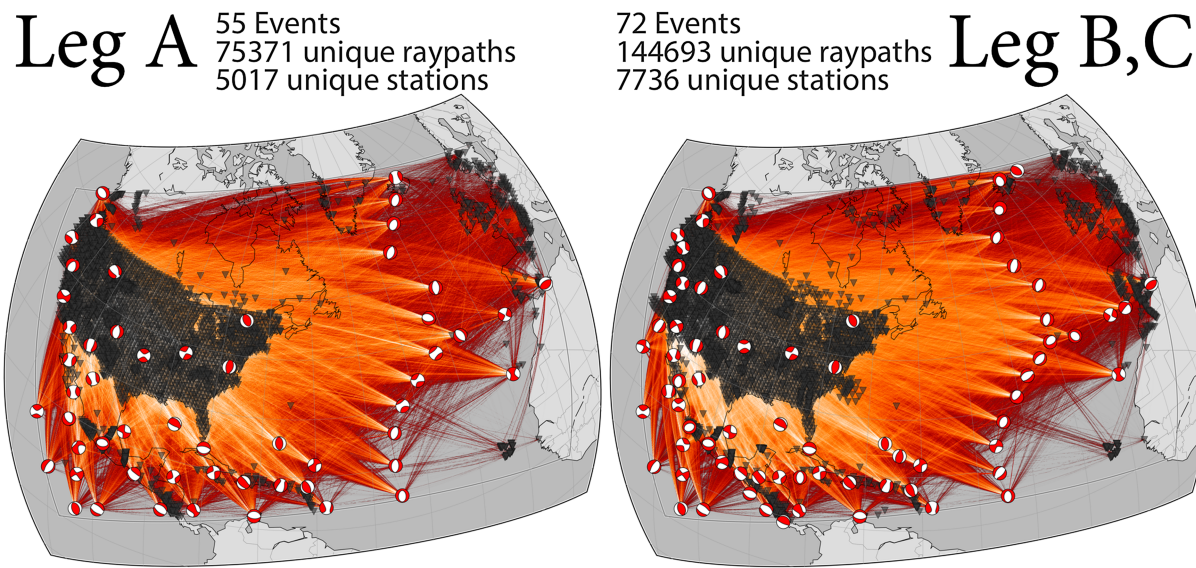


Figure 6. Surface-projected ray density plots of the events and stations for the different legs of the inversion. Note that we added more (and removed some) events when going from leg A to B. Earthquakes are represented by red and white moment tensor beach balls, stations by black triangles, and raypaths by red to white lines. The sensitivity of the measurements is not restricted to the raypaths, but this is still a useful proxy to judge the potential resolution of the final model.

to recover from them is crucial. Nonetheless, the workflow tool was able to run for several weeks and performed multiple iterations in a row without requiring human intervention. At failure points it only took a minor effort to analyze the cause, repair it, and continue the workflow.

3. Data

An explicit goal of this study has been to use the maximum amount of data possible, as the simulation cost for forward and adjoint runs does not depend on the number of receivers. Thus, using the maximum number of receivers is desirable. Following that reasoning, we restrict the study to only use earthquakes occurring since the USAArray project has been operating with a significant number of stations in 2005.

Observed waveforms need to be clearly recorded at frequencies matching the simulations at stations across the domain. This gives a practical lower limit for the magnitude of usable events of $M_W = 5.0$. The upper limit of $M_W = 6.5$ was empirically chosen to avoid unmodeled finite-source effects.

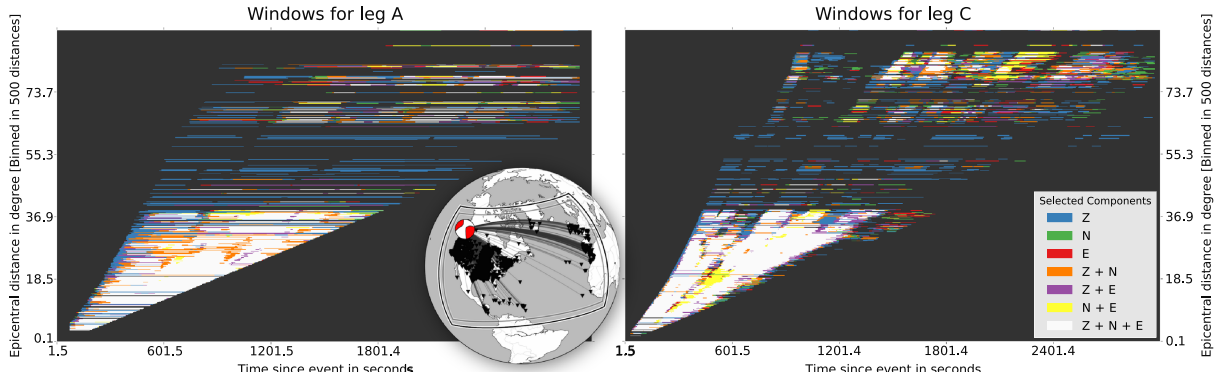


Figure 7. Statistical visualization of the automatically picked windows for a $M_W = 6.5$ event close to Vancouver Island in September 2011; for leg A (left panel) and for leg C (right panel). The windows were picked at the beginning of each leg to not change the misfit definition within one L-BFGS run. Both panels show which combinations of channels were picked for each epicentral distance as a function of passed time since the event. The windows were automatically picked by LASIF. The inset globe shows the event and recording stations. Stations with epicentral distances between about 40° to 60° are mostly noisy island stations, resulting in few window picks on the horizontal components.

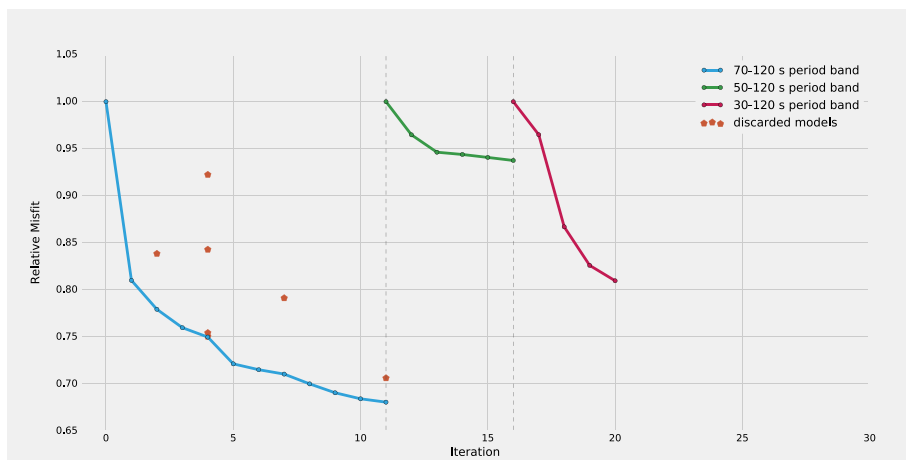


Figure 8. Misfit evolution and failed test models over the course of the inversion’s three legs. The orange-red pentagons denote discarded test models where the automatic step length determination of L-BFGS failed. The blue line denotes the misfit decrease during the 70–120 s leg A of the inversion, the green line the reduction during leg B with periods from 50 to 120 s, and the red line finally showing the misfit evolution during the computationally expensive leg C of the operation from 30 to 120 s. Misfits are relative to the misfit at the start of each leg. The initial model already had a good waveform fit, explaining the limited total reduction in the misfit.

The limited maximum magnitude is challenging for the first, longest-period leg of the inversion using periods from 70 to 120 s. Events with small magnitudes and thus small rupture surfaces may not excite sufficient long-period energy. Combined with frequently lacking instrumental sensitivity in these period ranges, this results in a smaller number of recordings, especially on the horizontal components.

In total, we selected 55 earthquakes from the global centroid-moment tensor (GCMT) catalog (Ekström et al., 2012) for leg A, and 72 for legs B and C. For the event selection, we optimized for the best possible spatial distribution of events to improve coverage. If no event has yet been chosen, the algorithm picks a random one. It then proceeds to choose that event from the whole remaining catalog that has the maximum distance to the next closest event. This ensures the selection of all events with rare locations and approximates a Poisson disc sampling in regions with many events. Choosing more events would not add significant new information as each new event would be close to an already existing one, assuming that earthquake mechanisms are predominantly determined by a region’s tectonics.

For each event we downloaded all freely accessible data from data centers worldwide, resulting in recordings from about 2,000 unique stations per event for legs B and C. The data sources are documented in Appendix A, and the total data coverage is illustrated in Figure 6.

The raw number of waveform traces prohibits manual control or visual inspection and thus has to be handled by automatic algorithms. Statistical plots like the one shown in Figure 7 are used to judge their behavior.

4. Results and Resolution Proxies

In the following paragraphs, we present the iterative model evolution, a detailed validation and resolution analysis, and an overview of the final model.

4.1. Model Evolution

We carried out 20 iterations over three legs as shown in Figure 8, each leg being a separate L-BFGS optimization run. For the longest-period leg A, at 70–120 s, we performed 11 iterations. We applied strong smoothing of the gradients to prevent the optimization procedure from getting trapped in a local minimum. Further iterations at 70 s would not have significantly improved the overall misfit.

For leg B, at a periods of 50–120 s, we only performed five iterations as the misfit evolution stagnated as seen in Figure 8. A potential cause for this may be an insufficiently small difference between simulations at 70 and at 50 s.

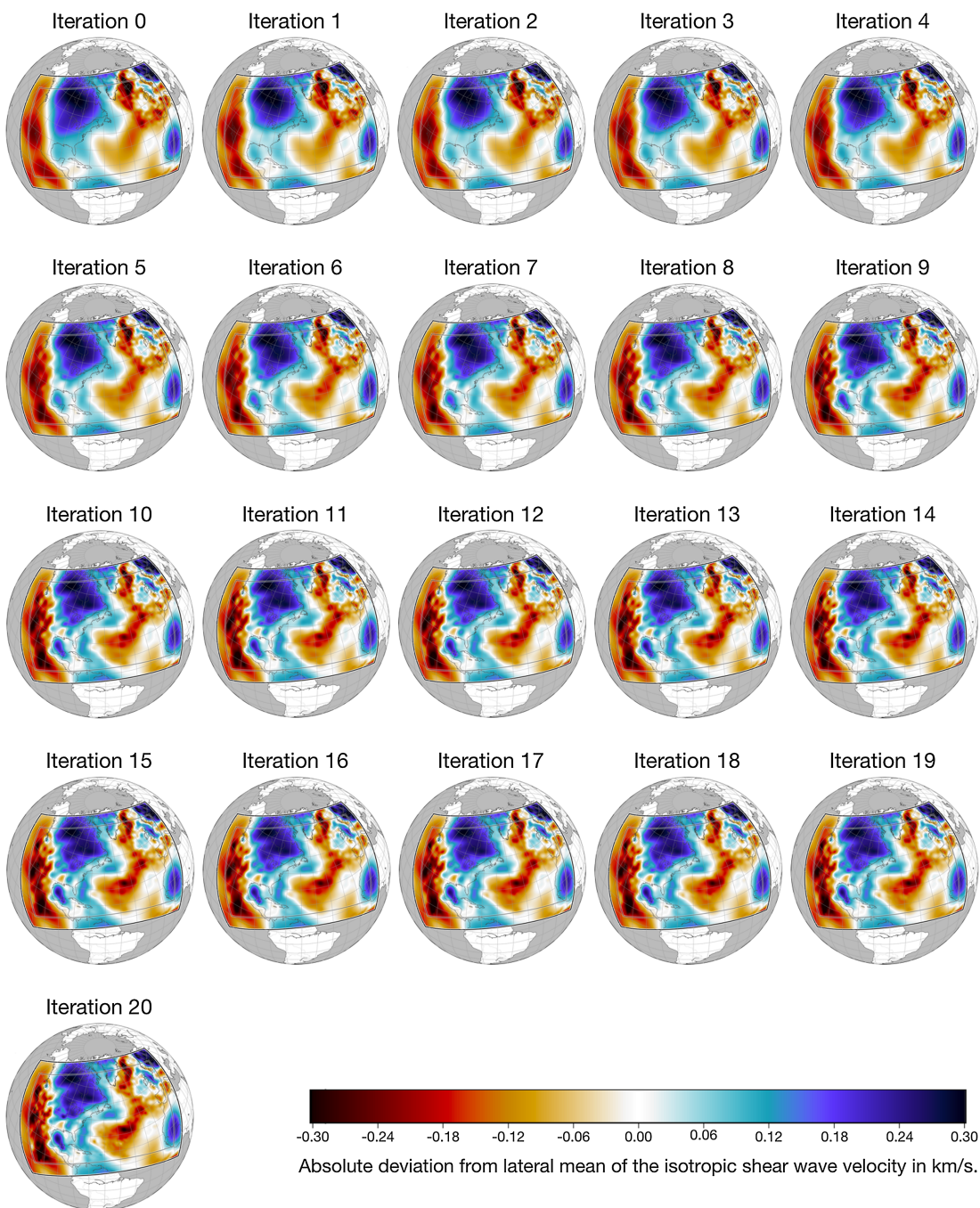


Figure 9. Horizontal slices of the model at every iteration. Shown are absolute deviations of the isotropic S velocity from the lateral mean at a depth of 150 km at a frequency of 1 Hz. The first iterations at long periods mostly adjust long-wavelength structure. Smaller details tend to appear during later iterations at shorter periods.

Simulations become significantly more expensive at periods from 30 to 120 s but do result in a fast and strong misfit reduction which only lasts for a single iteration before tapering off. We performed a few more iterations after iteration 20, which still decreased the total misfit. However, strong localized artifacts, mainly around the sources, started to appear. This led us to effectively terminate the inversion after the twentieth iteration.

The red pentagons in Figure 8 represent rejected test models that failed one of the Wolfe conditions (Nocedal & Wright, 2006). L-BFGS results in a natural step length of 1, under the assumption that the misfit is locally quadratic. For our nonlinear problem that is not always the case, thus leading to discarded test models.

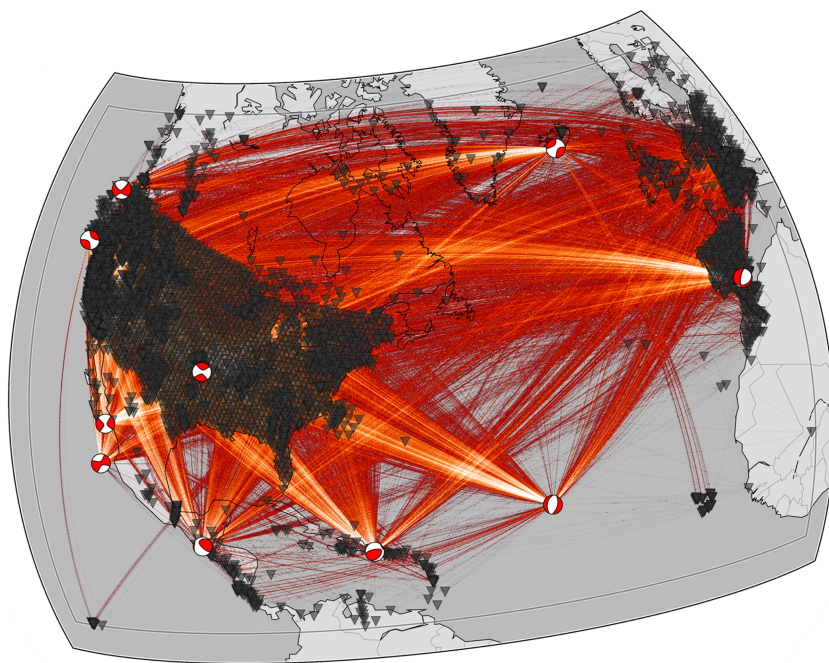


Figure 10. Map with 10 earthquakes of the validation data set that were not used in the inversion. Event locations and focal mechanisms are shown as red-white beach balls; the recording stations are depicted as black triangles. The data consist of 22,472 raypaths recorded on 6,166 unique stations, mostly on all three components.

A reduction of the step length was required in these cases to further reduce the misfit. The L-BFGS algorithm works well in the large-scale example studied in this work and mostly eliminates the need to perform an explicit and costly line search to determine a suitable step length. The simulations to test a candidate update immediately become the forward simulations of the next iteration, speeding up the process. The internal smoothing in the L-BFGS parameterization successfully avoids the need to restart the optimization algorithm that has been observed in other studies.

Figure 9 presents the model evolution with horizontal slices of isotropic shear wave speed (Voigt averaged $v_s = \sqrt{(2v_{sv} + v_{sh})/3}$) at a depth of 150 km for all iterations. As expected, the first iterations only change the large-scale structure, while later iterations keep adding more details. The gradient-based optimization scheme improves the models only slowly with small differences from iteration to iteration. Interestingly, large jumps in misfit value also do not coincide with big apparent changes in the model.

4.2. Validation

A validation data set is used to help gauge the quality of the final Earth model. It includes 10 earthquakes not used in the inversion and is shown in Figure 10. The data set contains 22,472 unique source-receiver raypaths recorded with mostly three components at 6,166 unique stations. The validation domain is slightly larger than the inversion domain and contains some new stations, most notably in Spain and Morocco, that were not available at the time when the inversion itself was performed. Thus, the validation data set contains independent pieces of data.

Synthetic seismograms with a duration of 3,000 s are calculated through the initial and the final model with a mesh accurate for periods of ~ 30 s. To test if the final model yields better synthetics, not just for the employed time-frequency phase misfit but for other measurements as well, we use a different measure. Inspired by Tape et al. (2010) and Simute et al. (2016), a normalized waveform difference L^2 misfit is used to compare data and synthetics on all three components with no prior windowing or selection aside from removing observed data traces with no visible earthquake signal. The misfit χ_{wf} is given by

$$\chi_{wf}(\mathbf{m}) = \frac{\int_0^T [u_{\text{obs}}(t) - u_{\text{syn}}(t, \mathbf{m})]^2 dt}{\sqrt{\int_0^T [u_{\text{obs}}(t)]^2 dt \int_0^T [u_{\text{syn}}(t, \mathbf{m})]^2 dt}}, \quad (2)$$

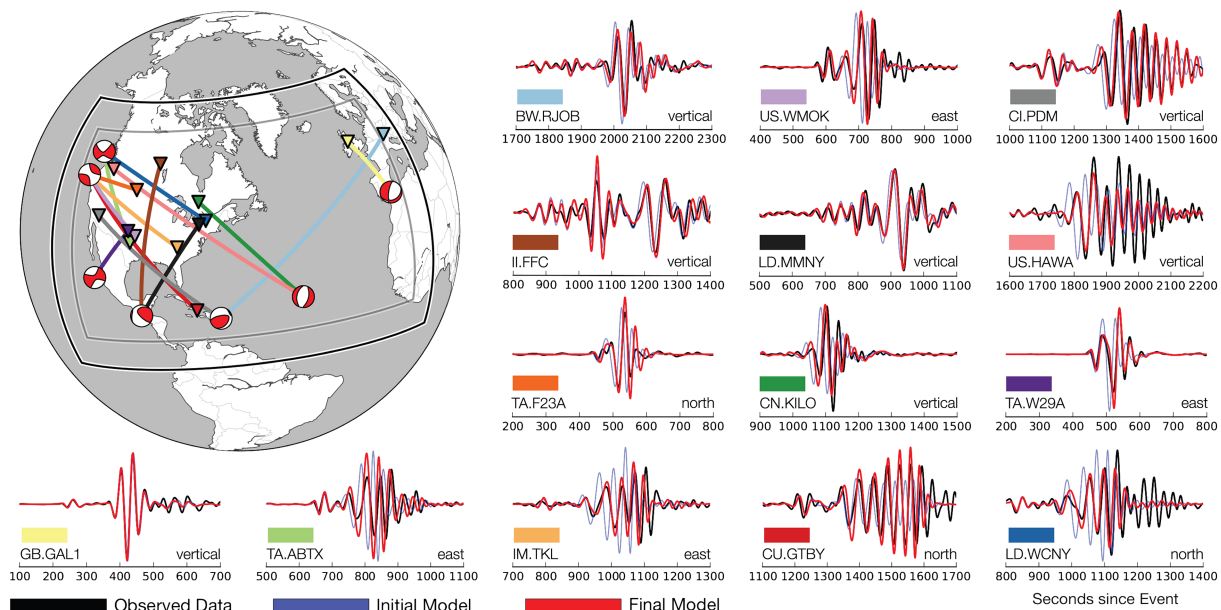


Figure 11. Representative waveform plots for some events from the validation data set, comparing seismograms calculated through the initial model to seismograms calculated through the final model. Raypath colors match the boxes next to the seismograms. Note that the waveforms for some stations, for example, for station GB.GAL1, basically did not change. This is due to the preexisting full-waveform inversion model for Europe.

where u_{obs} and u_{syn} are observed and corresponding synthetic waveform traces with data from time $t = 0$ (initial time) to $t = T$ (final time), and \mathbf{m} is the Earth model which the synthetic data depend on. Note that this measurement includes all parts of the seismograms, including late arriving and scattered wave energy that was not used for the inversion, and no amplitude normalization was applied.

Around 75% of all seismograms improve when comparing against observations, when going from the initial to the final model. Additionally, the summed misfit for each individual event decreases, indicating that the inversion indeed produced a generally improved Earth model. Figure 11 shows the waveform fit for events from the validation data set for the initial versus the final model.

4.3. Resolution Lengths

A more formal, quantitative resolution analysis is achieved via random probing, as introduced by Fichtner and van Leeuwen (2015). It yields position- and direction-dependent resolution lengths based on estimating the action of the Hessian on random test vectors. The resolution length is defined as the half-width of the point spread function in a certain direction, and it can be interpreted as the minimum required distance to distinguish two separate perturbations. The main idea of the method is that the action of the Hessian $H(\mathbf{m})$ on a perturbation $\delta\mathbf{m}$ can be interpreted as a conservative estimate of the point spread function. By applying random perturbations $\delta\mathbf{m}$ to a model and estimating $H(\mathbf{m})\delta\mathbf{m}$, its smoothing width in any direction can be estimated via autocorrelations. Averaging over five random models empirically yields stable resolution length estimates, shown in Figure 12.

In practice, the Hessian vector products $H(\mathbf{m})\delta\mathbf{m}$ were approximated using gradient differences, which corresponds to a finite-difference approximation of a second derivative by first derivatives.

The strongly heterogeneous source-receiver distribution results in an uneven resolution of the final model (see, e.g., Rawlinson et al., 2014; Yanovskaya, 1997). Resolution length in the vertical direction is roughly 3 times smaller than in the horizontal directions. This is an expected result of the surface wave dominance in the data set, and of the sensitivity distribution of surface waves. The uneven ray coverage in Figure 6 foreshadows an anisotropic resolution in the Northern Atlantic region due to the predominantly E-W traveling waves which is confirmed in the resolution analysis.

This resolution analysis is relevant only for the structure added during this inversion, and not for details already contained in the initial model, for instance, in central Europe (Fichtner et al., 2013).

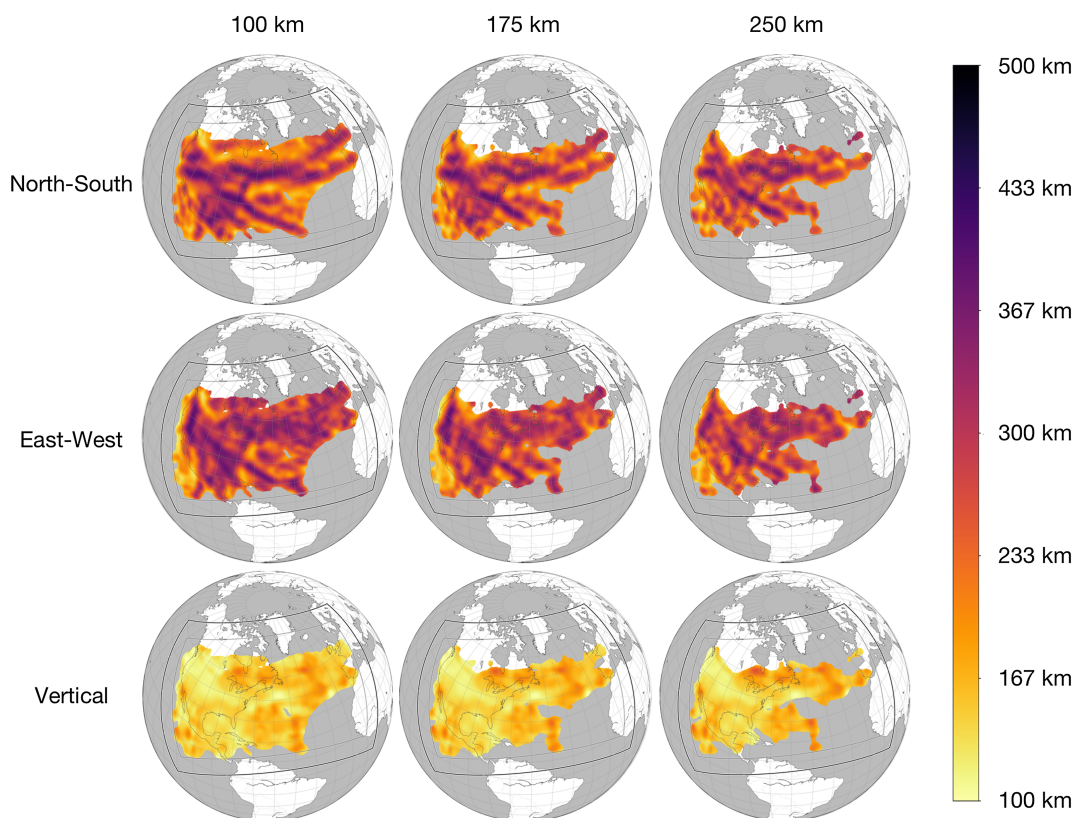


Figure 12. Position- and direction-dependent resolution lengths based on estimating the action of the Hessian on a random test vector calculated with the random probing technique of Fichtner and van Leeuwen (2015) for the final model. The top row shows resolution lengths approximately in north-south direction along the mesh boundaries, the center row in east-west direction, and the last row in the vertical direction. The columns are depth slices in 100-, 175-, and 250-km depth. No resolution estimates are shown in regions where the absolute sum of all considered kernels to estimate the Hessian is beneath a chosen threshold as these could not be interpreted. Generally, visible trends include the better vertical compared to horizontal resolution due to the dominant usage of surface waves in the inversion, better N-S resolution in large parts of the Northern Atlantic compared to the E-W resolution as expected from the dominantly E-W traveling waves in that region (compare to Figure 6), and a shrinking region of good data coverage with depth.

4.4. Final Model

Figures 13 and 14 show horizontal and vertical slices through the final model, respectively. Heterogeneities with respect to the lateral mean decrease with depth in absolute as well as relative terms. Modifications of the initial crustal structure are, as expected for these periods, rather mild, and will thus not be discussed explicitly.

An encouraging result is that the final model in Europe does not significantly differ from the initial model. The final model continues preexisting detailed features into the low-resolution region of the initial model, which is best visible along the Mid-Atlantic Ridge. As previously mentioned, the initial model's European part originated from a previous full-waveform inversion operating in a similar period band (Fichtner et al., 2013) but with a different data set and partially different methodology. We did not treat the European region of the model any different to the rest of the domain. The same is true for the part of the model including results from an inversion for the South Atlantic region (Colli et al., 2013), but, as we have no data there, this is trivially expected.

The lateral v_{sh} and v_{sv} velocity averages of the inversion domain relative to PREM (Dziewoński & Anderson, 1981), shown in Figure 15, offer another viewpoint. The final model's resolution is predominantly limited to the upper 300 km, which is in accord with using mostly surface waves. We also included body waves in the inversion where they could be measured, but their influence on the final model is limited. Teleseismic body waves travel deep, and they are largely absorbed by the bottom domain boundary. Furthermore, the initial

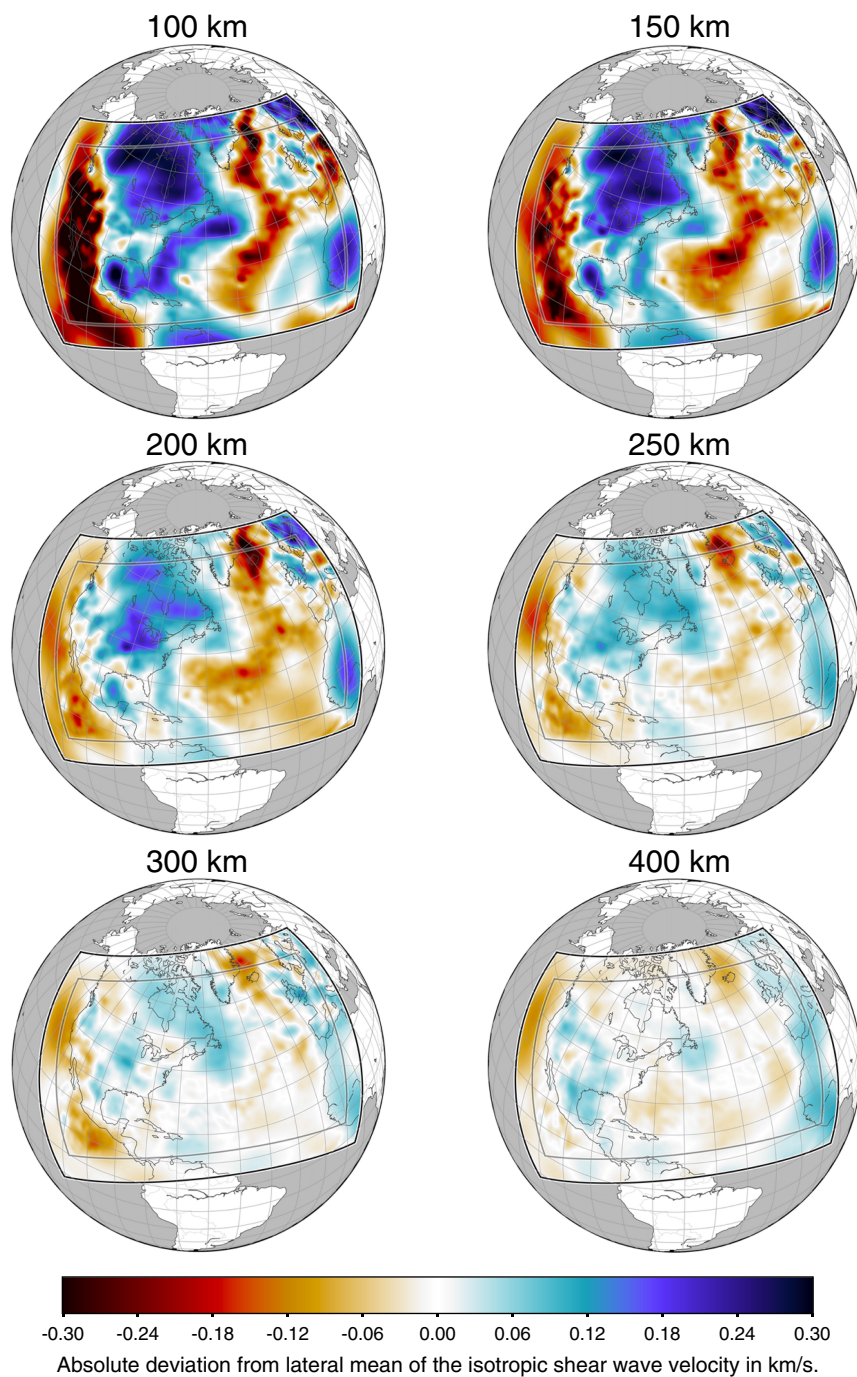


Figure 13. Horizontal slices through the final model showing the isotropic S velocity at various depths with the same color scale. The deviations from the lateral mean decrease with increasing depth, as expected.

model already explains long-period body waves rather well. In future studies, more sophisticated weighting schemes may be able to increase the influence of body waves.

Anisotropy in the initial model, except in the embedded high-resolution models, originates from PREM and is thus laterally constant with depth. Figure 16 plots the shear wave anisotropy $\zeta = \frac{v_{SH} - v_{SV}}{v_S} \times 100\%$ of the final versus the initial model. Laterally heterogeneous anisotropy in the model is required by the data. The uppermost mantle expectedly shows a predominantly positive shear wave anisotropy in the sense that v_{SH} is larger than v_{SV} .

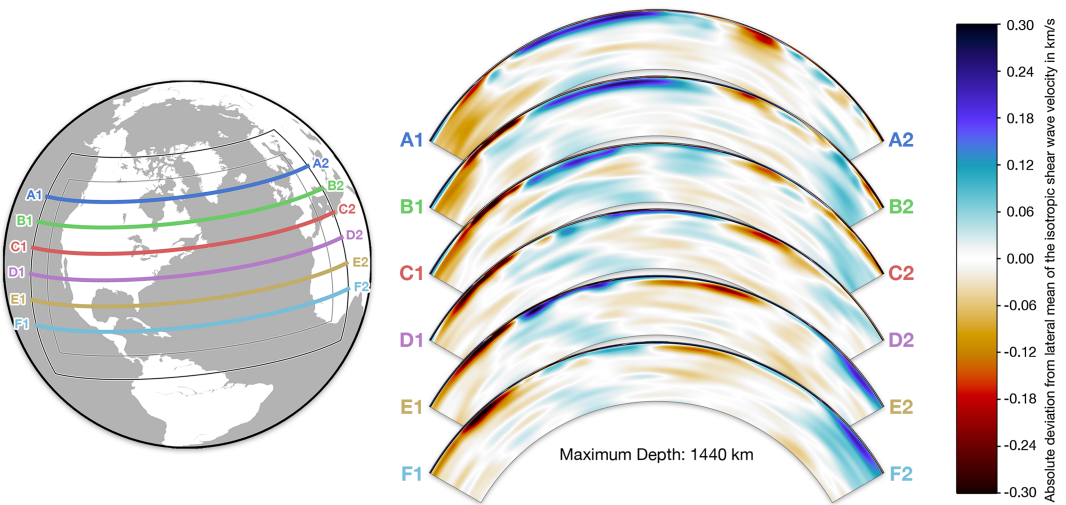


Figure 14. Roughly east-west oriented vertical slices of the isotropic S wave velocity of the final model in terms of absolute deviation from the lateral mean (right panel) from the surface to a maximum depth of 1,440 km. The left panel denotes the geographic location of the slices; the endpoints A1, A2, ..., F2 are shown in both panels.

4.5. Waveform Fit

The seismic velocity model produces synthetic seismograms that are objectively more similar to the observed data than seismograms calculated with the initial model. Figure 17 shows two exemplary three-component recordings compared to synthetics calculated with the initial model and the final model for the full duration of the simulations. Except for long-period coda waves arriving after the fundamental-mode surface waves, observations and synthetics match for every oscillation, in both phase and amplitude. Some oscillations of the seismograms from the initial model are cycle skipped and a meaningful phase misfit measurement would not have been possible if the inversion had started directly with the shortest periods.

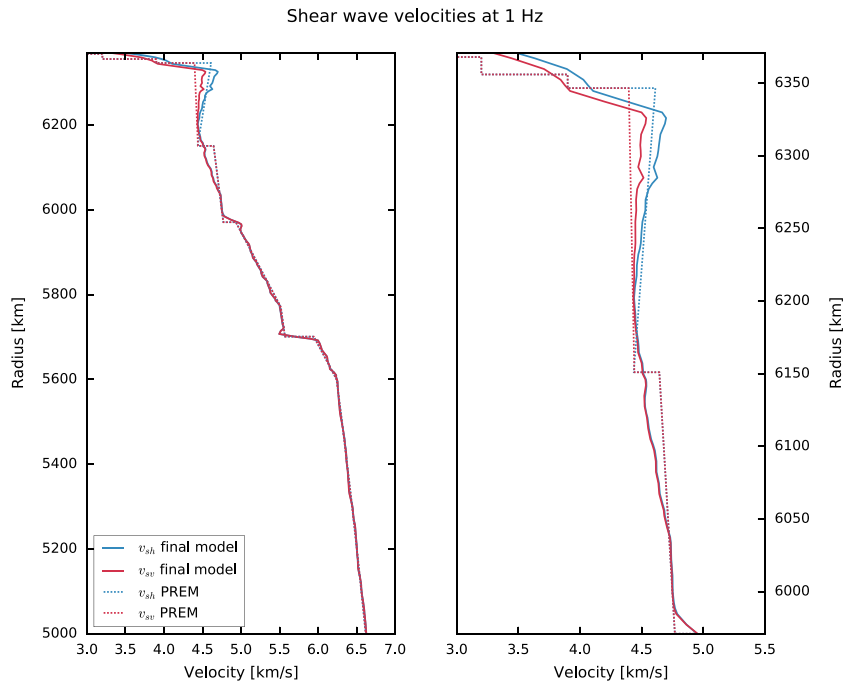


Figure 15. Lateral averages of the horizontally and vertically polarized shear wave velocities of the final model compared to Preliminary reference Earth model (PREM; Dziewoński & Anderson, 1981) at 1 Hz. The left panel shows the full depth extent of the model, the right one a zoom into the upper 400 km. Note the different axes. The 220-km discontinuity has been smoothed out in the initial model.

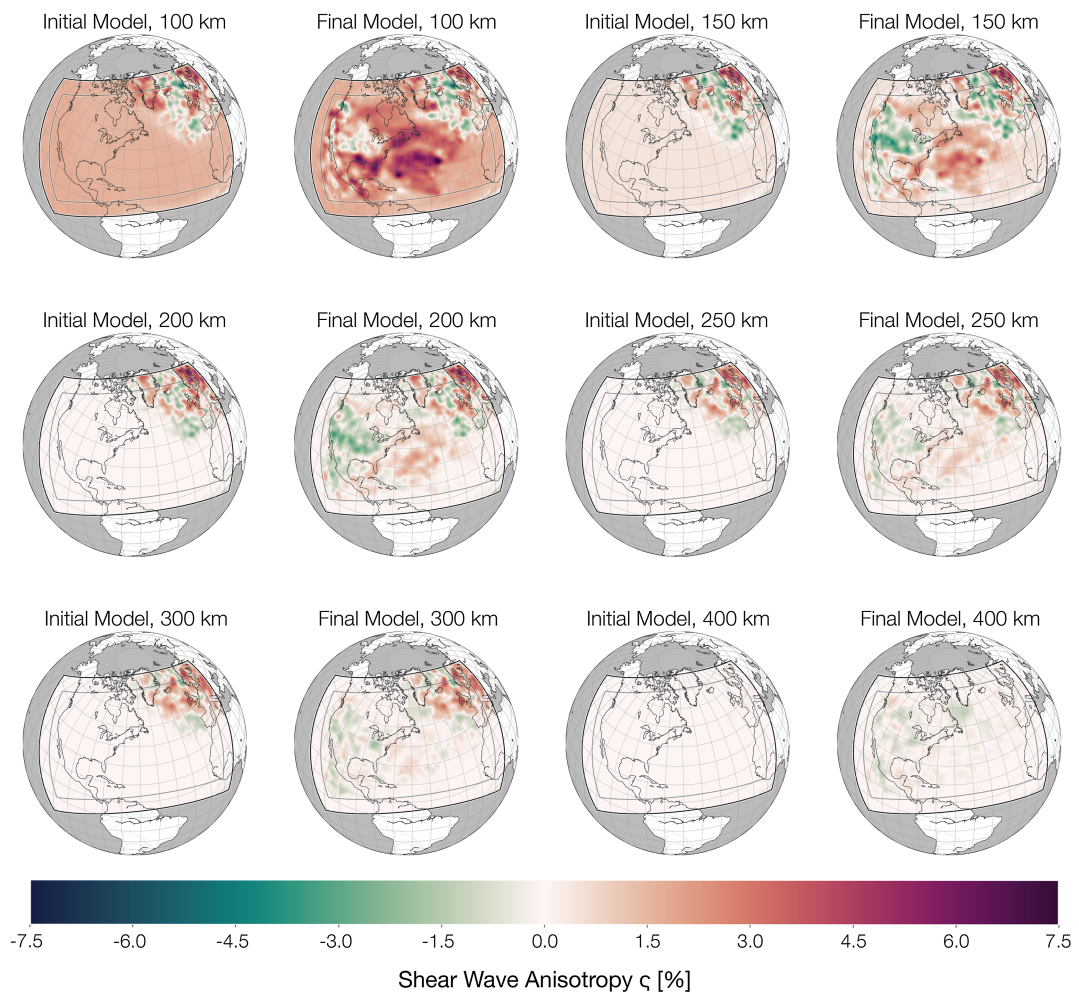


Figure 16. Horizontal slices of radial shear wave anisotropy $\xi = \frac{v_{SH}-v_{SV}}{v_s} \times 100\%$ of the initial versus the final model for a number of depths. Red colors denote regions where v_{SH} is larger than v_{SV} and green colors the opposite. The initial model has a constant radial anisotropy except in regions with existing high-resolution models. Additional laterally heterogeneous anisotropy is thus required to explain the data.

5. Discussion

This study focusses exclusively on the development of the large-scale waveform inversion method, and on the construction and validation of the seismic velocity model. A geologic/tectonic interpretation is work in progress and will be the subject of future publications.

It is important to understand that the inversion results, including the validation and resolution analysis, are unavoidably affected by various types of observational and modeling errors that are hard to quantify and to take into account properly. These are discussed in the following paragraphs.

While we do employ an accurate numerical scheme to calculate forward and adjoint wavefields, which in theory yields accurate gradients, there are still a number of physical effects that we do not account for. Some can be safely neglected within our chosen period range, others should be accommodated in future studies.

Komatitsch and Tromp (2002) demonstrate how to add rotation, and self-gravitation to spectral-element simulations—we simulate neither of them, mainly for reasons of code complexity, practicality, and computational efficiency. Rotation has a small potential effect on the amplitudes which is of no further concern for this study as it uses a phase-only time-frequency misfit. Self-gravitation has the most profound effect on long-period waves, and its influence is only minor for the frequencies we invert. Including even lower frequencies would indeed necessitate self-gravitating waves.

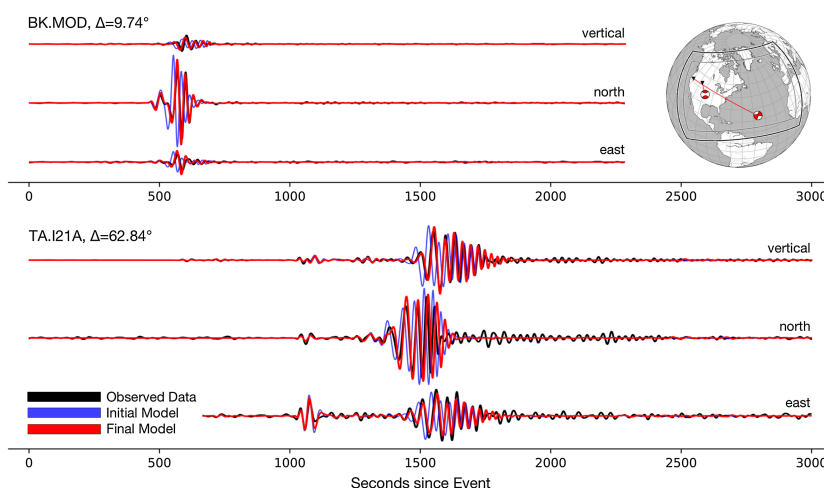


Figure 17. Exemplary waveform comparisons of synthetics through the initial and the final model simulated at a dominant period of 30 s against observed data. Amplitudes are not scaled. The inversion used windowed data, but these two examples show waveform traces for the full simulated duration. Surface waves are affected more strongly than body waves whose effect cannot be seen at this scale. Phases are improved throughout the whole data set; amplitudes are, in general, not significantly changed.

The effect of oceans is modeled via an effective crust computed by Backus averaging (Backus, 1962). If an approximation of the ocean by an effective load, as proposed by Komatitsch and Tromp (2002), provides a better solution seems to be an open question.

Our numerical mesh has some inaccuracies as well. It is a regular, spherical chunk and thus has no topography, ellipticity, nor internal boundaries. Topography and ellipticity have only minor influences for surface waves at long periods. Nuber et al. (2016) show the influence of topography on full-waveform inversions. They conclude that it does affect the final result but only for significant topography (defined as more than half the minimum wavelength), which our chosen inversion domain does not have. The most significant internal boundary in our inversion domain is the Moho. It is not honored by our mesh so the final inverted model has to be interpreted as an effective representation of the true crustal model for our mesh and frequency range that is required by the data (Backus, 1962; Capdeville, 2010; Fichtner & Igel, 2008). Explicitly meshing, and thereby fixing, poorly known internal discontinuities may have detrimental effects.

Further inaccuracies we do not take into account are errors of the observed data. These range from faulty sensors, inaccurate orientations, strong and local site effects, timing errors, wrong instrument responses, and other issues. This, as a whole, is a problem that is almost intractable as many subtle errors can only be detected by the network and data center operators, potentially with the help of projects like IRIS' MUSTANG (<http://service.iris.edu/mustang>, last accessed April 2017). Our quality control, as described in section 3, catches many of these by comparing observed to synthetic data, but subtly erroneous data will still enter the inversion. Using large amounts of data should reduce the effects of misbehaving seismograms. Properly quantifying and propagating data errors in full-waveform inversion will remain a challenge for the foreseeable future.

We also do not invert for the sources but assume the centroid-moment tensor solutions from the GCMT catalog (Ekström et al., 2012) to be correct. Our inversion domain is not global, meaning that any inversion for source mechanisms will likely incur a bias from imperfect azimuthal coverage especially for those events close to the domain boundary. This brings along a risk of overfitting the data. Bozdağ et al. (2016) perform a global full-waveform source inversion for 253 events from the GCMT catalog and find that they generally change little, usually less than 5 km in depth and less in the lateral directions. This is consistent with findings in Hjörleifsdóttir and Ekström (2010) who presents the results of synthetic tests for the accuracy of the GCMT catalog. Concluding, it might benefit the inversion to invert for some source parameters, most prominently the event depth, but the risk of a bias especially in restricted domains has to be accounted for. The frequency range of our inversion and the expected differences in event parameters would only result in a minor effect.

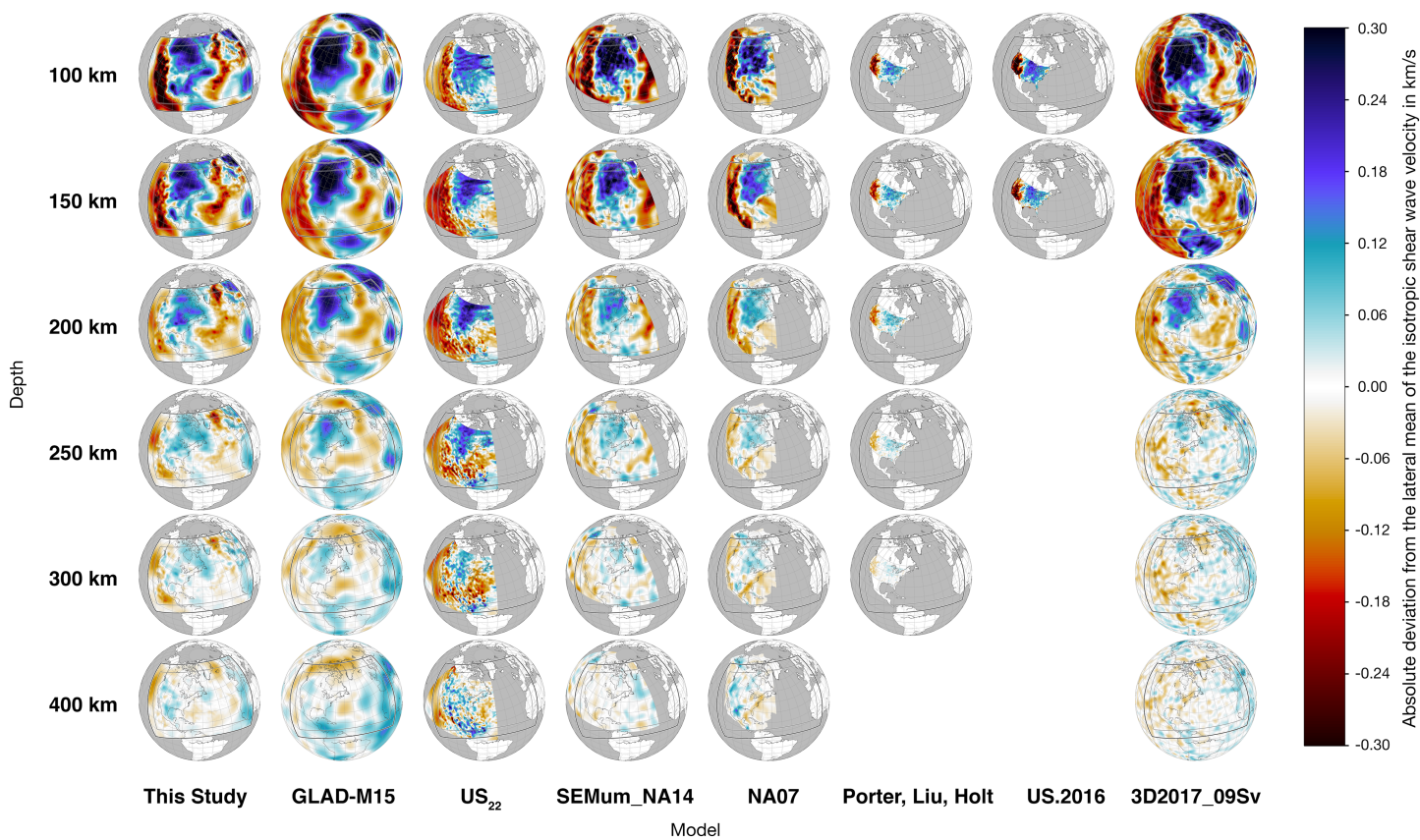


Figure 18. Comparison of the Voigt averaged or isotropic shear wave velocities of this study to a selection of other models. The color scale is identical for all plots, and the deviations are in reference to the lateral mean of each model at any given depth. Models range from regional to global scales and have been generated using full-waveform inversion with adjoint techniques similar to this study (*GLAD-M15*, Bozdağ et al., 2016; *US₂₂*, Zhu et al., 2017), full-waveform inversion with asymptotic gradients (*SEMum_NA14*, Yuan et al., 2014), by inverting for fundamental and higher-mode Rayleigh waveforms from vertical component seismograms using partitioned waveform inversion (*NA07*, Bedle & Van Der Lee, 2009), by inverting for Rayleigh wave phase velocities (*Porter, Liu, Holt*, Porter et al., 2016; *US.2016*; Shen & Ritzwoller, 2016 additionally inverted for group velocities), and by inverting for path-averaged shear velocities (*3D2017_09Sv*, Debayle et al., 2016, has its own reference model).

Various other studies constraining the (an)isotropic subsurface structure of the North American continent have been published in the past (e.g., Bedle & Van Der Lee, 2009; Nettles & Dziewoński, 2008; Schmandt & Lin, 2014; Sigloch, 2011; Yuan et al., 2014), the most similar to this work in terms of geographic domain and methodology is a recent model by Zhu et al. (2017). Figure 18 compares this study's model to a selection of existing models. The large-scale structure is in good agreement across models, whereas the fine-scale structure differs at times. This disparity is, at the time of writing, an unfortunate fact of seismic tomographies (see, e.g., Becker, 2012). More data coupled with new and better methods will hopefully result in models agreeing across all scales and the model presented in this manuscript contributes to that process.

6. Conclusions

We present a new full seismic waveform inversion model for North America and the Northern Atlantic, taking advantage of USArray data. The model was constructed using numerical forward and adjoint simulations with the spectral-element method coupled with a time-frequency domain phase misfit. Updates for 20 iterations were carried out using a Gaussian prior-preconditioned L-BFGS method. To judge the quality of the final model, we performed a validation test with new data and an independent misfit measurement and the final model improved the fit to the data for that data set. Additionally, we performed a quantitative resolution analysis before discussing the final model and its features.

A particular focus of this work has been on methodological and workflow developments to not only enable the creation of this model in the first place but to also facilitate future full-waveform inversions,

harnessing the ever growing computational and data resources. To this end we created a graph-based workflow framework that is capable of automatically orchestrating the inversion with minimal human intervention in a reliable and trustworthy manner.

Future work needs to find ways to further improve resolution without producing local artifacts. Incorporating more data, relocating events, and reducing forward modeling errors are the next steps. Another promising route would be to use more sophisticated data-weighting schemes, regularization techniques, and potentially preconditioners to handle the spatially strongly varying data availability. Weighting body wave measurements in a different manner would also allow for more resolution in greater depths. Exploiting the strong spatial clustering of seismic sources as well as receivers via special misfits and adjoint sources also has potential to improve the resolution (Yuan et al., 2016).

Appendix A: Gaussian Prior in L-BFGS

The raw gradient of the misfit functional often contains high-frequency artifacts and small-scale oscillations. It is common practice to eliminate those unwanted features by applying a smoothing operator to the gradient before updating the model. While this works well for steepest descent or conjugate gradient methods, extra care has to be taken for L-BFGS methods to ensure that the search direction using the smoothed gradient is still a direction of descent.

Consider a Gaussian prior \mathbf{G} , which is a positive definite linear operator. The Gaussian can be split up into $\mathbf{G} = \mathbf{G}^{\frac{1}{2}} \mathbf{G}^{\frac{1}{2}}$, where $\mathbf{G}^{\frac{1}{2}}$ is again a Gaussian smoothing kernel with smaller width.

To integrate the smoothing operation into L-BFGS, we change the parameterization within the inversion routine and introduce an auxiliary model $\hat{\mathbf{m}}$ such that $\mathbf{m} = \mathbf{G}^{\frac{1}{2}} \hat{\mathbf{m}}$. Hence,

$$\frac{\partial}{\partial \hat{\mathbf{m}}} \chi(\mathbf{m}) = \frac{\partial}{\partial \mathbf{m}} \chi(\mathbf{m}) \cdot \mathbf{G}^{\frac{1}{2}}. \quad (\text{A1})$$

Now, the L-BFGS update formula in the auxiliary model space is given by

$$\hat{\mathbf{m}}^{k+1} = \hat{\mathbf{m}}^k - \sigma \mathbf{H} \mathbf{G}^{\frac{1}{2}} \nabla \chi(\mathbf{m}^k), \quad (\text{A2})$$

where \mathbf{H} is the L-BFGS approximation of the inverse Hessian, σ is a suitable step length, and $\nabla \chi(\mathbf{m}^k)$ is the raw gradient of the misfit functional with respect to the physical model. By substituting the physical model \mathbf{m} into equation (A2), we finally arrive at

$$\mathbf{m}^{k+1} = \mathbf{m}^k - \sigma \mathbf{G}^{\frac{1}{2}} \mathbf{H} \mathbf{G}^{\frac{1}{2}} \nabla \chi(\mathbf{m}^k). \quad (\text{A3})$$

Equation (A3) contains the prior-preconditioned L-BFGS approximation $\mathbf{G}^{\frac{1}{2}} \mathbf{H} \mathbf{G}^{\frac{1}{2}}$, which ensures—by construction—that the search direction is a direction along which the misfit decreases.

There are two important things to note. First, for the steepest descent method, \mathbf{H} is the identity, and the model update simplifies to the smoothed negative gradient $-\mathbf{G} \nabla \chi(\mathbf{m}^k)$, scaled by σ . Second, when directly inserting the smoothed gradient into L-BFGS, the search direction would be $-\mathbf{H} \mathbf{G} \nabla \chi(\mathbf{m}^k)$, which is different from (A3) and not necessarily a direction of descent.

Appendix B: Data Acknowledgments

We acquired freely available data from data centers listed in the following together with the URLs (all last accessed March 2017) of their FDSN (Romanowicz & Dziewonski, 1986) compatible web services:

- Bundesanstalt für Geowissenschaften und Rohstoffe (BGR, Federal Institute for Geosciences and Natural Resources) in Hannover: <http://eida.bgr.de>
- Swiss Seismological Service (SED) at ETH Zurich: <http://eida.ethz.ch>
- Helmholtz Centre Potsdam - GFZ German Research Centre for Geosciences: <https://geofon.gfz-potsdam.de>
- Istituto nazionale di geofisica e vulcanologia (INGV): <http://webservices.rm.ingv.it>
- Institut de physique du globe de Paris (IPGP): <http://eida.ipgp.fr>
- Incorporated Research Institutions for Seismology Data Management Center (IRIS DMC): <http://service.iris.edu>

- Kandilli Observatory And Earthquake Research Institute (KOERI): <http://eida.koeri.boun.edu.tr>
- Ludwig-Maximilians-University Munich (LMU): <http://erde.geophysik.uni-muenchen.de>
- Northern California Earthquake Data Center (NCEDC): <http://service.ncedc.org>
- Observatories & Research Facilities for European Seismology (ORFEUS): <http://www.orfeus-eu.org>
- Réseau Sismologique et Géodesique Français (RESIF): <http://ws.resif.fr>
- Southern California Earthquake Data Center (SCEDC): <https://service.scedc.caltech.edu>

From these data centers we obtained waveforms and station meta-information from 140 permanent networks and 104 temporary deployments. Digital object identifiers (DOIs) are starting to be used to link to data from seismic networks in order to give credit where it is due (Evans et al., 2015). As best practices in this regard are not yet fully established and moving everything to the bibliography is impractical for data-heavy projects we are listing them here in alphabetical order, starting with the permanent networks:

- **AE**: Arizona Geological Survey (2009): Arizona Broadband Seismic Network. doi:10.7914/SN/AE
- **AF**: Penn State University (2004): AfricaArray. doi:10.7914/SN/AF
- **AK**: Alaska Earthquake Center, Univ. of Alaska Fairbanks (1987): Alaska Regional Network. doi:10.7914/SN/AK
- **AT**: NOAA National Oceanic and Atmospheric Administration (USA) (1967): National Tsunami Warning Center Alaska Seismic Network. doi:10.7914/SN/AT
- **AZ**: Frank Vernon, UC San Diego (1982): ANZA Regional Network. doi:10.7914/SN/AZ
- **BC**: Centro de Investigación Científica y de Educación Superior de Ensenada (CICESE), Ensenada (1980): Red Sísmica del Noroeste de México. doi:10.7914/SN/BC
- **BE**: Royal Observatory of Belgium (1985): Belgian Seismic Network. doi:10.7914/SN/BE
- **BK**: Northern California Earthquake Data Center. (2014). Berkeley Digital Seismic Network (BDSN) [Data set]. Northern California Earthquake Data Center. doi:10.7932/BDSN
- **CA**: Institut Cartogràfic i Geològic de Catalunya-Institut d'Estudis Catalans (1996): Catalan Seismic Network. doi:10.7914/SN/CA
- **CC**: Cascades Volcano Observatory/USGS (2004): Cascade Chain Volcano Monitoring. doi:10.7914/SN/CC
- **CH**: Swiss Seismological Service (SED) at ETH Zurich. (1983). National Seismic Networks of Switzerland. ETH Zürich. doi:10.12686/sed/networks/ch
- **CI**: California Institute of Technology (Caltech) (1926): Southern California Seismic Network. doi:10.7914/SN/CI
- **CO**: University of South Carolina (1987): South Carolina Seismic Network. doi:10.7914/SN/CO
- **CU**: Albuquerque Seismological Laboratory (ASL)/USGS (2006): Caribbean USGS Network. doi:10.7914/SN/CU
- **CZ**: Institute of Geophysics, Academy of Sciences of the Czech Republic (1973): Czech Regional Seismic Network. doi:10.7914/SN/CZ
- **DR**: Universidad Autónoma de Santo Domingo (ISU/UASD Dominican Republic) (1998): Centro Nacional de Sismología (CNS). doi:10.7914/SN/DR
- **EI**: Dublin Institute for Advanced Studies (1993): Irish National Seismic Network (INSN). doi:10.7914/SN/EI
- **FR**: RESIF. (1995). RESIF-RLBP French Broad-band network, RESIF-RAP strong motion network and other seismic stations in metropolitan France. RESIF - Réseau Sismologique et géodésique Français. doi:10.15778/RESIF.FR
- **G**: Institut de Physique du Globe de Paris (IPGP), & Ecole et Observatoire des Sciences de la Terre de Strasbourg (EOST). (1982). GEOSCOPE, French Global Network of broad band seismic stations. Institut de Physique du Globe de Paris (IPGP). doi:10.18715/GEOSCOPE.G
- **GE**: GEOFON Data Centre. (1993). GEOFON Seismic Network. Deutsches GeoForschungsZentrum GFZ. doi:10.14470/TR560404
- **GS**: Albuquerque Seismological Laboratory (ASL)/USGS (1980): US Geological Survey Networks. doi:10.7914/SN/GS
- **GU**: University of Genova (1967): Regional Seismic Network of North Western Italy. doi:10.7914/SN/GU
- **IB**: Institute Earth Sciences "Jaume Almera" CSIC (ICTJA Spain) (2007): IberArray. doi:10.7914/SN/IB
- **IE**: Idaho National Laboratory (1972): INL Seismic Monitoring Program. doi:10.7914/SN/IE
- **II**: Scripps Institution of Oceanography (1986): IRIS/IDA Seismic Network. doi:10.7914/SN/II
- **IU**: Albuquerque Seismological Laboratory (ASL)/USGS (1988): Global Seismograph Network (GSN - IRIS/USGS). doi:10.7914/SN/IU

- **IV:** INGV Seismological Data Centre. (1997). Rete Sismica Nazionale (RSN). Istituto Nazionale di Geofisica e Vulcanologia (INGV), Italy. doi:10.13127/SD/X0FXnH7QFy
- **IW:** Albuquerque Seismological Laboratory (ASL)/USGS (2003): Intermountain West Seismic Network. doi:10.7914/SN/IW
- **KP:** Korea Polar Research Institute (KOPRI) (2013): Korea Polar Seismic Network. doi:10.7914/SN/KP
- **KY:** Kentucky Geological Survey/Univ. of Kentucky (1982): Kentucky Seismic and Strong Motion Network. University of Kentucky. doi:10.7914/SN/KY
- **LI:** California Institute of Technology (Caltech) (2000): Laser Interferometer Gravitational-Wave Experiment (LIGO). doi:10.7914/SN/LI
- **LO:** Instituto Politecnico Loyola (2012): Observatorio Sismológico Politécnico Loyola. doi:10.7914/SN/LO
- **MB:** Montana Bureau of Mines and Geology/Montana Tech (MBMG, MT USA) (2001): Montana Regional Seismic Network. doi:10.7914/SN/MB
- **MN:** MedNet project partner institutions. (1988). Mediterranean Very Broadband Seismographic Network (MedNet). Istituto Nazionale di Geofisica e Vulcanologia (INGV), Italy. doi:10.13127/SD/fBBBtDtd6q
- **N4:** UC San Diego (2013): Central and Eastern US Network. doi:10.7914/SN/N4
- **NC:** USGS Menlo Park (1967): USGS Northern California Network. doi:10.7914/SN/NC
- **NE:** Albuquerque Seismological Laboratory (ASL)/USGS (1994): New England Seismic Network. doi:10.7914/SN/NE
- **NI:** OGS (Istituto Nazionale di Oceanografia e di Geofisica Sperimentale) and University of Trieste (2002): North-East Italy Broadband Network. doi:10.7914/SN/NI
- **NN:** University of Nevada (UNR Reno) (1971): Nevada Seismic Network. doi:10.7914/SN/NN
- **NP:** USGS Earthquake Science Center (1931): United States National Strong-Motion Network. doi:10.7914/SN/NP
- **NU:** Nicaraguan Institute of Terristerial Studies (1992): Nicaraguan Seismic Network. doi:10.7914/SN/NU
- **NX:** Nanometrics Seismological Instruments (2013): Nanometrics Research Network. doi:10.7914/SN/NX
- **NY:** Pascal Audet, University of Ottawa (2013): Yukon-Northwest Seismic Network. doi:10.7914/SN/NY
- **OK:** Oklahoma Geological Survey (1978): Oklahoma Seismic Network. doi:10.7914/SN/OK
- **OO:** Rutgers University (2013): Ocean Observatories Initiative. doi:10.7914/SN/OO
- **OX:** OGS (Istituto Nazionale di Oceanografia e di Geofisica Sperimentale) (2016): North-East Italy Seismic Network. doi:10.7914/SN/OX
- **PE:** Penn State University (2004): Pennsylvania State Seismic Network. doi:10.7914/SN/PE
- **PR:** University of Puerto Rico (1986): Puerto Rico Seismic Network (PRSN) & Puerto Rico Strong Motion Program (PRSM). doi:10.7914/SN/PR
- **PY:** Frank Vernon, UC San Diego (2014): Piñon Flats Observatory (PFO) Array. doi:10.7914/SN/PY
- **RC:** Brigham Young Univ-Idaho (BYU Idaho) (2001): BYU-Idaho Network. doi:10.7914/SN/RC
- **RV:** Alberta Geological Survey / Alberta Energy Regulator (2013): Regional Alberta Observatory for Earthquake Studies Network. doi:10.7914/SN/RV
- **SL:** Slovenian Environment Agency (2001): Seismic Network of the Republic of Slovenia . doi:10.7914/SN/SL
- **SN:** University of Nevada (UNR Reno) (1995): Southern Great Basin Network. doi:10.7914/SN/SN
- **ST:** Geological Survey-Provincia Autonoma di Trento (1981): Trentino Seismic Network. doi:10.7914/SN/ST
- **TA:** IRIS Transportable Array (2003): USArray Transportable Array. doi:10.7914/SN/TA
- **TC:** Información de la Red Sismológica Nacional de Costa Rica. (n.d.). doi:10.15517/tc
- **TE:** Electricity Generating Authority of Thailand (2015): EGAT Dams Seismic Monitoring System. doi:10.7914/SN/TE
- **UP:** SNSN. (1904). Swedish National Seismic Network. Uppsala University, Uppsala, Sweden. doi:10.18159/SNSN
- **US:** Albuquerque Seismological Laboratory (ASL)/USGS (1990): United States National Seismic Network. doi:10.7914/SN/US
- **UU:** University of Utah (1962): University of Utah Regional Seismic Network. doi:10.7914/SN/UU
- **UW:** University of Washington (1963): Pacific Northwest Seismic Network. doi:10.7914/SN/UW
- **WI:** Institut de Physique du Globe de Paris- IPGP. (2008). GNSS, seismic broadband and strong motion permanent networks in West Indies. Institut de Physique du Globe de Paris - IPGP. doi:10.18715/antilles.WI
- **WM:** San Fernando Royal Naval Observatory (ROA), Universidad Complutense de Madrid (UCM), Helmholtz-Zentrum Potsdam Deutsches Geoforschungszentrum (GFZ), Universidade de Evora (UEVORA, P.),

& Institute Scientifique of RABAT ISRABAT, M. (1996). The Western Mediterranean BB seismic Network. Deutsches Geoforschungszentrum GFZ. doi:10.14470/JZ581150

- **WY:** University of Utah (1984): Yellowstone Wyoming Seismic Network. doi:10.7914/SN/WY

In addition, we used data from the following permanent seismic networks that did not yet have a DOI assigned at the time of writing: AG, AO, AR, AX, AY, BN, BW, CM, CN, CW, CY, DK, DZ, EB, EE, EP, ES, ET, GB, GI, GL, GR, HE, HF, HW, IM, IP, JM, LB, LC, LD, LX, MC, MG, MQ, MT, MX, NA, NL, NM, NO, NR, NS, NV, NW, OE, OV, PA, PB, PG, PL, PM, PN, PO, RD, RE, S, SB, SC, SE, SI, SS, SV, SX, TD, TH, TO, TR, TV, UK, UO, VE, VI, WC, WR, and WU.

Used temporary networks are postfixed with an underscore and the year of the deployment, again in alphabetical order:

- **2G_2010:** Bruce Douglas, Gary Pavlis, Jon Cameron (2010): Testing of the effectiveness of incorporating seismic data in seismic hazard assessment within a traditional field course. doi:10.7914/SN/2G_2010
- **3D_2010:** Christine Thomas (2010): Morocco-Muenster. doi:10.7914/SN/3D_2010
- **3E_2010:** Jer-Ming Chiu (2010): Exploring Seismic Velocity of Sediments in the Mississippi Embayment. doi:10.7914/SN/3E_2010
- **4F_2015:** Heather DeShon, Chris Hayward, Jacob Walter, M. Beatrice Magnani, Matthew Hornbach, Brian Stump (2015): North Texas Earthquake Study: Venus (Johnson County), TX. doi:10.7914/SN/4F_2015
- **5A_2010:** John Nabelek (2010): Crustal-Scale Geometry of Active Continental Normal Faults. doi:10.7914/SN/5A_2010
- **5E_2014:** Anne Trehu (2014): Cascadia Initiative. doi:10.7914/SN/5E_2014
- **7A_2013:** Maureen Long, Paul Wiita (2013): Mid-Atlantic Geophysical Integrative Collaboration. doi:10.7914/SN/7A_2013
- **7D_2009:** Wes Thelen, Paul Bodin (2009): Yakima Landslide RAMP. doi:10.7914/SN/7D_2009
- **7D_2011:** IRIS OBSIP (2011): Cascadia Initiative Community Experiment - OBS Component. doi:10.7914/SN/7D_2011
- **7E_2006:** Wilde-Piórko, M., Geissler, W. H., Plomerová, J., Knapmeyer-Endrun, B., Grad, M., Babuška, V., Wiejacz, P. (2006). PASSEQ 2006-2008: Passive Seismic Experiment in Trans-European Suture Zone. Deutsches Geoforschungszentrum GFZ. <https://doi:10.14470/2R383989>
- **9D_2010:** Roman Motyka, Mark Fahnstock, Martin Truffer (2010): Ice-ocean interaction at Nuuk tidewater glaciers. doi:10.7914/SN/9D_2010
- **X4_2016:** Recep Cakir (2016): Active Fault Mapping. doi:10.7914/SN/X4_2016
- **X8_2012:** William Menke, Vadim Levin, Fiona Darbyshire (2012): Deep Structure of Three Continental Sutures in Eastern North America. doi:10.7914/SN/X8_2012
- **X9_2008:** Brian Stump, Chris Hayward (2008): Dallas Earthquake Swarm. doi:10.7914/SN/X9_2008
- **XA_2008:** Anne Trehu, Mark Williams (2008): Monitoring seismicity associated with a possible asperity on the Cascadia megathrust. doi:10.7914/SN/XA_2008
- **XB_2009:** Alan Levander, Gene Humphreys, Pat Ryan (2009): Program to Investigate Convective Alboran Sea System Overturn. doi:10.7914/SN/XB_2009
- **XB_2014:** Robert Woodward, Dan Hollis, Neil Spriggs (2014): Sweetwater Array. doi:10.7914/SN/XB_2014
- **XC_2006:** David James, Matthew Fouch (2006): Collaborative Research: Understanding the causes of continental intraplate tectonomagmatism: A case study in the Pacific Northwest. doi:10.7914/SN/XC_2006
- **XD_2011:** Simon Klemperer (2011): Passive seismic study of a magma-dominated rift: the Salton Trough. doi:10.7914/SN/XD_2011
- **XD_2014:** Ken Creager (2014): Collaborative Research: Illuminating the architecture of the greater Mount St. Helens magmatic systems from slab to surface. doi:10.7914/SN/XD_2014
- **XE_2005:** Tom Owens, Craig Jones (2005): Sierra Nevada EarthScope Project. doi:10.7914/SN/XE_2005
- **XE_2012:** Paul Bodin (2012): Seismic Activity of Low Angle Normal Faults in Death Valley, California. doi:10.7914/SN/XE_2012
- **XF_2006:** Steve Grand, Jim Ni (2006): Mapping the Rivera Subduction Zone. doi:10.7914/SN/XF_2006
- **XG_2009:** Ken Creager, John Vidale, Steve Malone (2009): Cascadia Array of Arrays. doi:10.7914/SN/XG_2009
- **XI_2011:** Suzan van der Lee, Douglas Wiens, Michael Wysession, Justin Revenaugh, Seth Stein, Andrew Frederiksen, Fiona Darbyshire, Donna Jurdy, Patrick Shore (2011): Superior Province Rifting Earthscope Experiment. doi:10.7914/SN/XI_2011
- **XI_2014:** Mitchell Barklage (2014): Long Beach Broadband or LA Syncline Seismic Interferometry Experiment. doi:10.7914/SN/XI_2014

- **XJ_2008:** Glenn Biasi (2008): Wells, Nevada Aftershock Recording. doi:10.7914/SN/XJ_2008
- **XN_2008:** Alan Levander (2008): Bolivar: Western Venezuela. doi:10.7914/SN/XN_2008
- **XN_2010:** Anne Trehu, Mark Williams (2010): Monitoring seismicity associated with a possible asperity on the Cascadia megathrust. doi:10.7914/SN/XN_2010
- **XN_2011:** Kasper van Wijk (2011): joint summer field camp BSU/CSM/Imperial College of London. doi:10.7914/SN/XN_2011
- **XO_2011:** Gary Pavlis, Hersh Gilbert (2011): Ozark Illinois Indiana Kentucky (OIINK) Flexible Array Experiment. doi:10.7914/SN/XO_2011
- **XP_2008:** Ken Dueker, Rick Aster (2008): Colorado Rockies Experiment and Seismic Transect. doi:10.7914/SN/XP_2008
- **XQ_2006:** Yong-Gang Li, John Vidale (2006): Collaborative Research: Understanding Fault Zone Compliance by Seismic Probing of InSAR Anomalies. doi:10.7914/SN/XQ_2006
- **XQ_2007:** Alan Levander (2007): Seismic and Geodetic Investigations of Mendocino Triple Junction Dynamics. doi:10.7914/SN/XQ_2007
- **XQ_2012:** Lara Wagner (2012): Pre-Hydrofracking Regional Assessment of Central Carolina Seismicity. doi:10.7914/SN/XQ_2012
- **XR_2008:** Jay Pulliam, Steve Grand, Judy Sansom (2008): Seismic Investigation of Edge Driven Convection Associated with the Rio Grande Rift. doi:10.7914/SN/XR_2008
- **XT_2009:** Gregory P Waite (2009): Fuego Volcano 2009. doi:10.7914/SN/XT_2009
- **XT_2011:** Ray Russo (2011): Western Idaho Shear Zone - Passive. doi:10.7914/SN/XT_2011
- **XU_2006:** Steve Malone, Ken Creager, Stephane Rondenay, Tim Melbourne, Geoffrey Abers (2006): Collaborative Research: Earthscope integrated investigations of Cascadia subduction zone tremor, structure and process. doi:10.7914/SN/XU_2006
- **XU_2014:** Anne Sheehan (2014): Greeley Colorado RAMP Deployment 2014. doi:10.7914/SN/XU_2014
- **XU_2016:** Anne Sheehan (2016): USGS NEHRP Proposal 2016-0180 - Greeley. doi:10.7914/SN/XU_2016
- **XV_2009:** Anne Sheehan, Kate Miller, Megan Anderson, Christine Smith Siddoway, Eric Erslev (2009): Collaborative Research: Geometry and kinematics of basement-involved foreland arches: Insights into continental processes from Earthscope. doi:10.7914/SN/XV_2009
- **XY_2005:** Ken Dueker, George Zandt (2005): Magma Accretion and the Formation of Batholiths. doi:10.7914/SN/XY_2005
- **XY_2011:** Martin Chapman (2011): Experiment to Determine Hypocenters and Focal Mechanisms of Earthquakes Occurring in Association with Imaged Faults Near Summerville, South Carolina. doi:10.7914/SN/XY_2011
- **Y2_2013:** University of Bristol (2013): Balcombe. doi:10.7914/SN/Y2_2013
- **Y3_2008:** Glenn Biasi (2008): Wells, Nevada Aftershock Recording. doi:10.7914/SN/Y3_2008
- **Y7_2009:** Kasper van Wijk, Mike Batzle, Lee Liberty, Andre Revil (2009): Geothermal Exploration Arkansas Valley. doi:10.7914/SN/Y7_2009
- **Y8_2009:** Charles Langston, Heather DeShon (2009): Detection and location of non-volcanic tremor in the New Madrid Seismic Zone. doi:10.7914/SN/Y8_2009
- **YB_2005:** Gregory P Waite (2005): Mount Saint Helens Dense Array. doi:10.7914/SN/YB_2005
- **YC_2011:** Anne Meltzer (2011): RAMP Virginia. doi:10.7914/SN/YC_2011
- **YD_2008:** John Louie (2008): Recording Mogul Events throughout the Reno Basin. doi:10.7914/SN/YD_2008
- **YE_2008:** Jamie Steidl (2008): Title: NEESR-SG: High Fidelity site characterization by experimentation, field observation, and inversion-based modeling. doi:10.7914/SN/YE_2008
- **YE_2011:** Bruce Beaudoin, Tim Parker, Eliana Arias-Dotson (2011): Testing TA & FA vaults and directly buried sensor (3T). doi:10.7914/SN/YE_2011
- **YG_2012:** Anne Trehu, Geoffrey Abers (2012): Collaborative Research: Imaging the Cascadia subduction zone - a ship-to-shore opportunity. doi:10.7914/SN/YG_2012
- **YH_2008:** Rebecca Saltzer, Gene Humphreys (2008): LaBarge Experiment. doi:10.7914/SN/YH_2008
- **YO_2014:** Gaherty, James B., Laura Wagner, Anne Becel, Margaret Benoit, Maureen Long, Donna Shillington, Harm Van Avendonck, Brandon Dugan (2014): Eastern North American Margin Community Seismic Experiment. doi:10.7914/SN/YO_2014
- **YQ_2009:** David Hawthorn (2009): Lincoln Noise Study. doi:10.7914/SN/YQ_2009
- **YW_2005:** Ken Creager (2005): Stalking Cascadia episodic tremor and slip with enhanced GPS and seismic arrays. doi:10.7914/SN/YW_2005

- **YW_2016:** Kent Anderson, Justin Sweet, Bob Woodward (2016): IRIS Community Wavefield Experiment in Oklahoma. Incorporated Research Institutions for Seismology. doi:10.7914/SN/YW_2016
- **YX_2008:** James Cochran, Yong-Gang Li, Jamie Steidl (2008): Seismology Rapid Response Test During the SoSAF Shakeout. doi:10.7914/SN/YX_2008
- **YX_2010:** Simon Klemperer, Kate Miller (2010): Collaborative Research: 4D multi-disciplinary investigation of highly variable crustal response to continental extension in the north-central Basin and Range. doi:10.7914/SN/YX_2010
- **YY_2012:** Jake Walter (2012): Mendenhall Glacier Outburst Flood Seismicity and Next-Generation Instrument Testing. doi:10.7914/SN/YY_2012
- **YZ_2009:** Susan Y. Schwartz, Andrew Newman, Marino Protti, Victor Gonzalez (2009): Nicoya Seismogenic Zone. doi:10.7914/SN/YZ_2009
- **Z3_2009:** Silver (2009): Detecting Structural changes During an ETS Event: Proof of Concept. doi:10.7914/SN/Z3_2009
- **Z3_2010:** Shari Kelley, Greg Kaufman, Michael Albrecht (2010): Jemez Pueblo geothermal project. doi:10.7914/SN/Z3_2010
- **Z5_2013:** John Nabelek, Jochen Braunmiller (2013): Seismicity, Structure and Dynamics of the Gorda Deformation Zone. doi:10.7914/SN/Z5_2013
- **Z9_2010:** Karen M. Fischer, Robert B. Hawman, Lara S. Wagner (2010): Southeastern Suture of the Appalachian Margin Experiment. doi:10.7914/SN/Z9_2010
- **ZA_2006:** Michael West (2006): The Colima Deep Seismic Experiment: Imaging the Magmatic Root of Colima Volcano. doi:10.7914/SN/ZA_2006
- **ZH_2010:** Anne Sheehan, Kate Miller, Megan Anderson, Christine Smith Siddoway, Eric Erslev (2010): Collaborative Research: Geometry and kinematics of basement-involved foreland arches: Insights into continental processes from Earthscope. doi:10.7914/SN/ZH_2010
- **ZH_2011:** Anne Trehu, Mark Williams (2011): Monitoring seismicity associated with a possible asperity on the Cascadia mega-thrust. doi:10.7914/SN/ZH_2011
- **ZI_2010:** Kate Miller, Anne Sheehan, Megan Anderson, Christine Smith Siddoway, Eric Erslev, Steven Harder (2010): Collaborative Research: Geometry and kinematics of basement-involved foreland arches: Insights into continental processes from Earthscope. doi:10.7914/SN/ZI_2010
- **ZO_2010:** Diana Roman, Peter La_Femina (2010): Volcanic stress field analysis using non-local seismic sources at Hekla Volcano, Iceland. doi:10.7914/SN/ZO_2010
- **ZQ_2013:** Harold Gurrola (2013): Imaging the Matador arch using receiver functions from Texan dataloggers and short period geophones. doi:10.7914/SN/ZQ_2013
- **ZS_2009:** Sridhar Anandakrishnan (2009): CReSIS. doi:10.7914/SN/ZS_2009
- **ZW_2013:** Heather DeShon, Chris Hayward, Brian Stump, M. Beatrice Magnani, Matthew Hornbach (2013): North Texas Earthquake Study: Azle and Irving/Dallas. doi:10.7914/SN/ZW_2013
- **ZZ_2012:** Anne Trehu, Geoffrey Abers (2012): Collaborative Research: Imaging the Cascadia subduction zone - a ship-to-shore opportunity. doi:10.7914/SN/ZZ_2012

Temporary deployments without an assigned DOI at the time of writing that were utilized for this chapter are as follows: 2D_2010, 4E_2010, 4F_2007, 6A_2008, 7A_2010, 7F_2010, 8A_2010, X4_2010, X5_2007, X9_2012, XG_2014, XI_2005, XT_2006, XW_2013, XY_2013, Y9_2009, YB_2010, YC_2013, YF_2006, YF_2010, YY_2005, Z2_2006, Z2_2009, Z3_2008, Z4_2009, ZH_2016, ZN_2006, and ZX_2005.

References

- Afanasiev, M., Peter, D., Sager, K., Simute, S., Ermert, L., Krischer, L., & Fichtner, A. (2016). Foundations for a multiscale collaborative Earth model. *Geophysical Journal International*, 204(1), 39–58.
- Aki, K., Christoffersson, A., & Husebye, E. S. (1977). Determination of the three-dimensional seismic structure of the lithosphere. *Journal of Geophysical Research*, 82, 227–296.
- Anderson, J. E., Tan, L., & Wang, D. (2012). Time-reversal checkpointing methods for RTM and FWI. *Geophysics*, 77(4), S93–S103.
- Backus, G. E. (1962). Long-wave elastic anisotropy produced by horizontal layering. *Journal of Geophysical Research*, 67(11), 4427–4440.
- Bamberger, A., Chavent, G., Hemons, C., & Lailly, P. (1982). Inversion of normal incidence seismograms. *Geophysics*, 47, 757–770.
- Bamberger, A., Chavent, G., & Lailly, P. (1977). Une application de la théorie du contrôle à un problème inverse sismique. *Annales Geophysicae*, 33, 183–200.
- Becker, T. W. (2012). On recent seismic tomography for the western United States. *Geochemistry, Geophysics, Geosystems*, 13, Q01W10. <https://doi.org/10.1029/2011GC003977>

- Bedle, H., & Van Der Lee, S. (2009). *S* velocity variations beneath North America. *Journal of Geophysical Research*, 114, B07308. <https://doi.org/10.1029/2008JB005949>
- Beyreuther, M., Barsch, R., Krischer, L., Megies, T., Behr, Y., & Wassermann, J. (2010). ObsPy: A python toolbox for seismology. *Seismological Research Letters*, 81(3), 530–533.
- Bird, P. (2003). An updated digital model of plate boundaries. *Geochemistry, Geophysics, Geosystems*, 4(3), 1027. <https://doi.org/10.1029/2001GC000252>
- Blom, N., Boehm, C., & Fichtner, A. (2017). Synthetic inversions for density using seismic and gravity data. *Geophysical Journal International*, 209(2), 1204–1220. <https://doi.org/10.1093/gji/ggx076>
- Bodin, T., & Sambridge, M. (2009). Seismic tomography with the reversible jump algorithm. *Geophysical Journal International*, 178(3), 1411–1436. <https://doi.org/10.1111/j.1365-246X.2009.04226.x>
- Boehm, C., Hanzich, M., de la Puente, J., & Fichtner, A. (2016). Wavefield compression for adjoint methods in full-waveform inversion. *Geophysics*, 81(6), R385–R397.
- Bozdağ, E., Peter, D., Lefebvre, M., Komatitsch, D., Tromp, J., Hill, J., et al. (2016). Global adjoint tomography: First-generation model. *Geophysical Journal International*, 207(3), 1739–1766.
- Bozdağ, E., Trampert, J., & Tromp, J. (2011). Misfit functions for full waveform inversion based on instantaneous phase and envelope measurements. *Geophysical Journal International*, 185(2), 845–870.
- Bunks, C., Saleck, F. M., Zaleski, S., & Chavent, G. (1995). Multiscale seismic waveform inversion. *Geophysics*, 60, 1457–1473.
- Capdeville, Y. (2010). 1-D non-periodic homogenization for the seismic wave equation. *Geophysical Journal International*, 181, 897–910.
- Chen, P., Zhao, L., & Jordan, T. H. (2007). Full 3D tomography for the crustal structure of the Los Angeles region. *Bulletin of the Seismological Society of America*, 97, 1094–1120.
- Colli, L., Fichtner, A., & Bunge, H.-P. (2013). Full waveform tomography of the upper mantle in the South Atlantic region: Imaging a westward fluxing shallow asthenosphere? *Tectonophysics*, 604, 26–40.
- Çubuk Sabuncu, Y., Taymaz, T., & Fichtner, A. (2017). 3-D crustal velocity structure of western Turkey: Constraints from full waveform tomography. *Physics of the Earth and Planetary Interiors*, 270, 90–112.
- Dahlen, F., Hung, S.-H., & Nolet, G. (2000). Fréchet kernels for finite-frequency traveltimes—I. Theory. *Geophysical Journal International*, 141, 157–174.
- Debayle, E., Dubuffet, F., & Durand, S. (2016). An automatically updated *S*-wave model of the upper mantle and the depth extent of azimuthal anisotropy. *Geophysical Research Letters*, 43, 674–682. <https://doi.org/10.1002/2015GL067329>
- Dziewoński, A. M., & Anderson, D. L. (1981). Preliminary reference Earth model. *Physics of the Earth and Planetary Interiors*, 25(4), 297–356.
- Dziewoński, A. M., Hager, B. H., & O'Connell, R. J. (1977). Large-scale heterogeneities in the lower mantle. *Journal of Geophysical Research*, 82, 239–255.
- Ekström, G., Nettles, M., & Dziewoński, A. M. (2012). The global CMT project 2004–2010: Centroid-moment tensors for 13,017 earthquakes. *Physics of the Earth and Planetary Interiors*, 200–201, 1–9.
- Evans, P. L., Strollo, A., Clark, A., Ahern, T., Newman, R., Clinton, J. F., et al. (2015). Why seismic networks need digital object identifiers. *Eos*, 96. Retrieved from <https://eos.org/opinions/why-seismic-networks-need-digital-object-identifiers>
- Faccioli, E., Maggio, F., Paolucci, R., & Quarteroni, A. (1997). 2D and 3D elastic wave propagation by a pseudo-spectral domain decomposition method. *Journal of Seismology*, 1(3), 237–251.
- Fichtner, A. (2011). *Full seismic waveform modelling and inversion*. Berlin, Heidelberg: Springer.
- Fichtner, A., Bunge, H.-P., & Igel, H. (2006). The adjoint method in seismology I. Theory. *Physics of the Earth and Planetary Interiors*, 157(1–2), 86–104.
- Fichtner, A., & Igel, H. (2008). Efficient numerical surface wave propagation through the optimization of discrete crustal models—A technique based on non-linear dispersion curve matching (DCM). *Geophysical Journal International*, 173, 519–533.
- Fichtner, A., Kennett, B. L. N., Igel, H., & Bunge, H.-P. (2009). Full seismic waveform tomography for upper-mantle structure in the Australasian region using adjoint methods. *Geophysical Journal International*, 179, 1703–1725.
- Fichtner, A., Trampert, J., Cupillard, P., Saygin, E., Taymaz, T., Capdeville, Y., & Villaseñor, A. (2013). Multiscale full waveform inversion. *Geophysical Journal International*, 194, 534–556.
- Fichtner, A., & van Leeuwen, T. (2015). Resolution analysis by random probing. *Journal of Geophysical Research: Solid Earth*, 120, 5549–5573. <https://doi.org/10.1002/2015JB012106>
- French, S. W., & Romanowicz, B. (2014). Whole-mantle radially anisotropic shear velocity structure from spectral-element waveform tomography. *Geophysical Journal International*, 199, 1303–1327. <https://doi.org/10.1093/gji/ggu334>
- Friederich, W. (2003). The *S*-velocity structure of the East Asian mantle from inversion of shear and surface waveforms. *Geophysical Journal International*, 153, 88–102.
- Gokhberg, A., & Fichtner, A. (2016). Full-waveform inversion on heterogeneous HPC systems. *Computers & Geosciences*, 89, 260–268.
- Griewank, A. (1992). Achieving logarithmic growth of temporal and spatial complexity in reverse automatic differentiation. *Optimization Methods and Software*, 1(1), 35–54.
- Hjörleifsdóttir, V., & Ekström, G. (2010). Effects of three-dimensional Earth structure on CMT earthquake parameters. *Physics of the Earth and Planetary Interiors*, 179, 178–190.
- Igel, H., Djikpessé, H., & Tarantola, A. (1996). Waveform inversion of marine reflection seismograms for *P* impedance and Poisson's ratio. *Geophysical Journal International*, 124(2), 363–371.
- Jones, E., Oliphant, T., & Peterson, P. (2001–). SciPy: Open source scientific tools for Python. [Online; accessed November 1st, 2017].
- Koelemeijer, P., Deuss, A., & Ritsema, J. (2017). Density structure of Earth's lowermost mantle from Stoneley mode splitting observations. *Nature Communications*, 8, 1–10. <https://doi.org/10.1038/ncomms15241>
- Komatitsch, D. (1997). Méthodes spectrales et éléments spectraux pour l'équation de l'élastodynamique 2D et 3D en milieu hétérogène (PhD thesis), Institut de Physique du Globe de Paris.
- Komatitsch, D., & Tromp, J. (2002). Spectral-element simulations of global seismic wave propagation—II. Three-dimensional models, oceans, rotation and self-gravitation. *Geophysical Journal International*, 150, 308–318.
- Krischer, L., Fichtner, A., Zukauskaite, S., & Igel, H. (2015). Large-scale seismic inversion framework. *Seismological Research Letters*, 86(4), 1198–1207.
- Krischer, L., Megies, T., Barsch, R., Beyreuther, M., Lecocq, T., Caudron, C., & Wassermann, J. (2015). ObsPy: A bridge for seismology into the scientific Python ecosystem. *Computational Science & Discovery*, 8(1), 14,003–14,020.
- Krischer, L., Smith, J., Lei, W., Lefebvre, M., Ruan, Y., Andrade, E. S. D., et al. (2016). An adaptable seismic data format. *Geophysical Journal International*, 207(2), 1003–1011.

- Li, X. B., & Romanowicz, B. (1996). Global mantle shear velocity model developed using nonlinear asymptotic coupling theory. *Journal of Geophysical Research*, 101, 11,245–22,271.
- Liu, D. C., & Nocedal, J. (1989). On the limited memory BFGS method for large scale optimization. *Mathematical Programming*, 45(1–3), 503–528.
- Luo, Y., & Schuster, G. T. (1991). Wave-equation traveltime inversion. *Geophysics*, 56, 645–653.
- Megies, T., Beyreuther, M., Barsch, R., Krischer, L., & Wassermann, J. (2011). ObsPy—What can it do for data centers and observatories? *Annals Of Geophysics*, 54(1), 47–58.
- Meier, U., Curtis, A., & Trampert, J. (2007). Global crustal thickness from neural network inversion of surface wave data. *Geophysical Journal International*, 169(2), 706–722.
- Modrak, R., & Tromp, J. (2016). Seismic waveform inversion best practices: regional, global, and exploration test cases. *Geophysical Journal International*, 206(3), 1864–1889.
- Nettles, M., & Dziewoński, A. M. (2008). Radially anisotropic shear velocity structure of the upper mantle globally and beneath North America. *Journal of Geophysical Research*, 113, B02303. <https://doi.org/10.1029/2006JB004819>
- Nocedal, J., & Wright, S. (2006). *Numerical optimization* (2nd ed.). New York: Springer.
- Nuber, A., Manukyan, E., & Maurer, H. (2016). Ground topography effects on near-surface elastic full waveform inversion. *Geophysical Journal International*, 207(1), 67–71.
- Porter, R., Liu, Y., Holt, W. E., & Lithospheric records of orogeny within the continental U.S. (2016). *Geophysical Research Letters*, 43, 144–153. <https://doi.org/10.1002/2015GL066950>
- Prieux, V., Brossier, R., Operto, S., & Virieux, J. (2013). Multiparameter full waveform inversion of multicomponent ocean-bottom-cable data from the Valhall field. Part 1: Imaging compressional wave speed, density and attenuation. *Geophysical Journal International*, 194, 1640–1664.
- Rawlinson, N., Fichtner, A., Cambridge, M., & Young, M. K. (2014). Seismic tomography and the assessment of uncertainty. *Advances in Geophysics*, 55, 1–76.
- Ricker, F., Fichtner, A., & Trampert, J. (2012). Imaging mantle plumes with instantaneous phase measurements of diffracted waves. *Geophysical Journal International*, 190(1), 650–664.
- Ricker, F., Fichtner, A., & Trampert, J. (2013). The Iceland-Jan Mayen plume system and its impact on mantle dynamics in the North Atlantic region: Evidence from full-waveform inversion. *Earth and Planetary Science Letters*, 367, 39–51.
- Ritsema, J., Deuss, A., van Heijst, H., & Woodhouse, J. H. (2011). S4ORTS: A degree-40 shear-velocity model for the mantle from new Rayleigh wave dispersion, teleseismic traveltimes and normal-mode splitting function measurements. *Geophysical Journal International*, 184(3), 1223–1236. <https://doi.org/10.1111/j.1365-246X.2010.04884.x>
- Ritsema, J., & van Heijst, H. J. (2002). Constraints on the correlation of P- and S-wave velocity heterogeneity in the mantle from P, PP, PPP and PKPab traveltimes. *Geophysical Journal International*, 149, 482–489.
- Ritsema, J., Van Heijst, H. J., & Woodhouse, J. H. (1999). Complex shear velocity structure imaged beneath Africa and Iceland. *Science*, 286(5446), 1925–1928.
- Romanowicz, B., & Dziewoński, A. (1986). Toward a federation of broadband seismic networks. *EOS*, 67(25), 24–26.
- Cambridge, M., & Drijkoningen, G. (1992). Genetic algorithms in seismic waveform inversion. *Geophysical Journal International*, 109, 323–342.
- Schmandt, B., & Lin, F.-C. (2014). P and S wave tomography of the mantle beneath the United States. *Geophysical Research Letters*, 41, 6342–6349. <https://doi.org/10.1002/2014GL061231>
- Seriani, G., Priolo, E., & Pregaz, A. (1995). Modelling waves in anisotropic media by a spectral element method. In *Proceedings of the 3rd International Conference on Mathematical and Numerical Aspects of Wave Propagation* (pp. 289–298). Philadelphia, PA.
- Shen, W., & Ritzwoller, M. H. (2016). Crustal and uppermost mantle structure beneath the United States. *Journal of Geophysical Research: Solid Earth*, 121, 4306–4342. <https://doi.org/10.1002/2016JB012887>
- Sigloch, K. (2011). Mantle provinces under North America from multifrequency P wave tomography. *Geochemistry, Geophysics, Geosystems*, 12, Q02W08. <https://doi.org/10.1029/2010GC003421>
- Sigloch, K., McQuarrie, N., & Nolet, G. (2008). Two-stage subduction history under North America inferred from multiple-frequency tomography. *Nature Geoscience*, 1(7), 458–462.
- Simute, S., Steptoe, H., Cobden, L., Gokhberg, A., & Fichtner, A. (2016). Full-waveform inversion of the Japanese islands region. *Journal of Geophysical Research: Solid Earth*, 121, 3722–3741. <https://doi.org/10.1002/2016JB012802>
- Sukhovich, A., Bonnivier, S., Hello, Y., Irisson, J.-O., Simons, F. J., & Nolet, G. (2015). Seismic monitoring in the oceans by autonomous floats. *Nature Communications*, 6, 8027.
- Symes, W. W. (2007). Reverse time migration with optimal checkpointing. *Geophysics*, 72(5), SM213–SM221. <https://doi.org/10.1190/1.2742686>
- Tape, C., Liu, Q., Maggi, A., & Tromp, J. (2010). Seismic tomography of the southern California crust based on spectral-element and adjoint methods. *Geophysical Journal International*, 180(1), 433–462.
- Tape, C., Liu, Q., & Tromp, J. (2007). Finite-frequency tomography using adjoint methods—Methodology and examples using membrane surface waves. *Geophysical Journal International*, 168, 1105–1129.
- Tarantola, A. (1988). Theoretical background for the inversion of seismic waveforms, including elasticity and attenuation. *Pure and Applied Geophysics*, 128, 365–399.
- Thomson, D. (1982). Spectrum estimation and harmonic analysis. *Proceedings of the IEEE*, 70, 1055–1096.
- Tromp, J., Tape, C., & Liu, Q. (2005). Seismic tomography, adjoint methods, time reversal and banana-doughnut kernels. *Geophysical Journal International*, 160, 195–216.
- Wächter, A., & Biegler, L. T. (2005). On the implementation of an interior-point filter line-search algorithm for large-scale nonlinear programming. *Mathematical Programming*, 106(1), 1–33.
- Yanovskaya, T. B. (1997). Resolution estimation in the problems of seismic ray tomography. *Izvestiya, Physics of the Solid Earth*, 33, 76–80.
- Yomogida, K. (1992). Fresnel zone inversion for lateral heterogeneities in the Earth. *Pure and Applied Geophysics*, 138, 391–406.
- Yoshizawa, K., & Kennett, B. L. N. (2004). Multimode surface wave tomography for the Australian region using a three-stage approach incorporating finite frequency effects. *Journal of Geophysical Research*, 109, B02310. <https://doi.org/10.1029/2002JB002254>
- Yoshizawa, K., & Kennett, B. L. N. (2005). Sensitivity kernels for finite-frequency surface waves. *Geophysical Journal International*, 162, 910–926.
- Yuan, H., French, S., Cupillard, P., & Romanowicz, B. (2014). Lithospheric expression of geological units in central and eastern North America from full waveform tomography. *Earth and Planetary Science Letters*, 402(C), 176–186. <https://doi.org/10.1016/j.epsl.2013.11.057>

- Yuan, Y. O., Simons, F. J., & Tromp, J. (2016). Double-difference adjoint seismic tomography. *Geophysical Journal International*, 206(3), 1599–1618.
- Zhu, H., Bozdağ, E., Peter, D., & Tromp, J. (2012). Structure of the European upper mantle revealed by adjoint tomography. *Nature Geoscience*, 5(7), 493–498.
- Zhu, H., Komatitsch, D., & Tromp, J. (2017). Radial anisotropy of the North American upper mantle based on adjoint tomography with USArray. *Geophysical Journal International*, 211, 349–377.